Cell Reports

Article

Dihydroceramide desaturase regulates the compartmentalization of Rac1 for neuronal oxidative stress

Graphical abstract

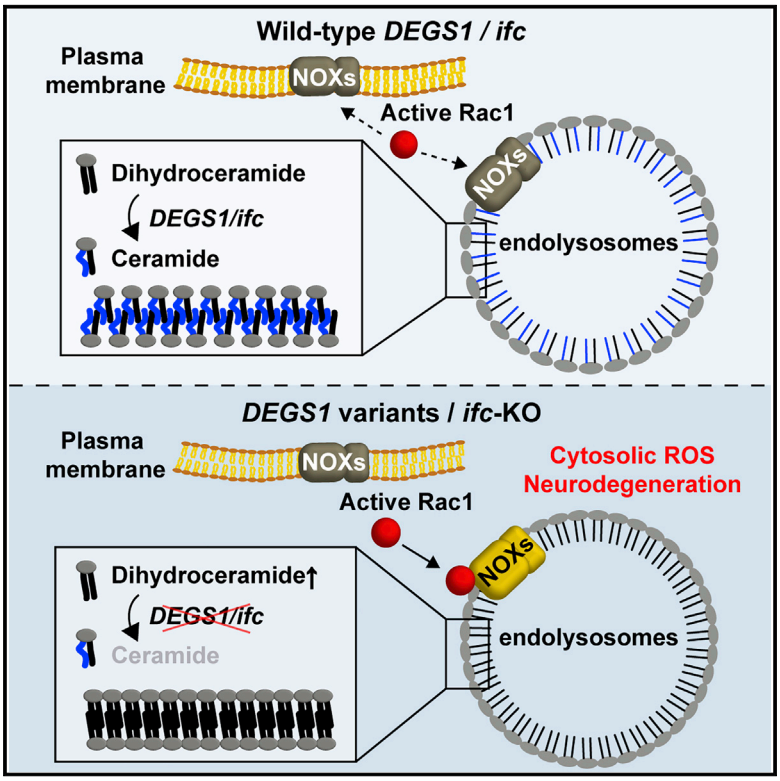

Authors

Fei-Yang Tzou, Tsu-Yi Su, Wan-Syuan Lin, ..., Ching-Hua Kuo, Shu-Yi Huang, Chih-Chiang Chan

Correspondence

chancc1@ntu.edu.tw

In brief

Deficient dihydroceramide desaturase activity causes oxidative stress-mediated neurological disorders. Tzou et al. show that dihydroceramide accumulation leads to mislocalization of active Rac1, and inhibition of Rac1-NOX can ameliorate associated oxidative stress and neuronal defects. Thus, NOX inhibitors may provide a therapeutic approach for patients with *DEGS1* variants.

Highlights

- Lack of dihydroceramide desaturase activity induces cytoplasmic ROS
- Rac1-NADPH oxidase-elicited ROS mediates leukodystrophy-related neuronal death
- *DEGS1/ifc* defects cause mislocalization of Rac1 to the endolysosomes
- Dihydroceramide alters binding of active Rac1 to reconstituted organelle membranes

Tzou et al., 2021, Cell Reports *35*, 108972
April 13, 2021
https://doi.org/10.1016/j.celrep.2021.108972

CellPress

Cell Reports

CellPress
OPEN ACCESS

Article

Dihydroceramide desaturase regulates the compartmentalization of Rac1 for neuronal oxidative stress

Fei-Yang Tzou,[1,4] Tsu-Yi Su,[1,4] Wan-Syuan Lin,[1] Han-Chun Kuo,[2] Yu-Lian Yu,[1] Yu-Han Yeh,[1] Chung-Chih Liu,[1] Ching-Hua Kuo,[2] Shu-Yi Huang,[3] and Chih-Chiang Chan[1,5,*]

[1]Graduate Institute of Physiology, College of Medicine, National Taiwan University, Taipei 100, Taiwan
[2]School of Pharmacy, College of Medicine, National Taiwan University, Taipei 100, Taiwan
[3]Department of Medical Research, National Taiwan University Hospital, Taipei 100, Taiwan
[4]These authors contributed equally
[5]Lead contact
*Correspondence: chancc1@ntu.edu.tw
https://doi.org/10.1016/j.celrep.2021.108972

SUMMARY

Disruption of sphingolipid homeostasis is known to cause neurological disorders, but the mechanisms by which specific sphingolipid species modulate pathogenesis remain unclear. The last step of *de novo* sphingolipid synthesis is the conversion of dihydroceramide to ceramide by dihydroceramide desaturase (human DEGS1; *Drosophila* Ifc). Loss of *ifc* leads to dihydroceramide accumulation, oxidative stress, and photoreceptor degeneration, whereas human *DEGS1* variants are associated with leukodystrophy and neuropathy. In this work, we demonstrate that *DEGS1/ifc* regulates Rac1 compartmentalization in neuronal cells and that dihydroceramide alters the association of active Rac1 with organelle-mimicking membranes. We further identify the Rac1-NADPH oxidase (NOX) complex as the major cause of reactive oxygen species (ROS) accumulation in *ifc*-knockout (*ifc*-KO) photoreceptors and in SH-SY5Y cells with the leukodystrophy-associated $DEGS1^{H132R}$ variant. Suppression of Rac1-NOX activity rescues degeneration of *ifc*-KO photoreceptors and ameliorates oxidative stress in $DEGS1^{H132R}$-carrying cells. Therefore, we conclude that *DEGS1/ifc* deficiency causes dihydroceramide accumulation, resulting in Rac1 mislocalization and NOX-dependent neurodegeneration.

INTRODUCTION

Sphingolipids, such as ceramide, are major components of neuronal membrane bilayers and are pivotal to the function of neurons. The last step of ceramide *de novo* synthesis is catalyzed by dihydroceramide desaturase (DEGS), which uses dihydroceramide as a substrate. Neuronal dihydroceramide is less abundant than ceramide (Qin et al., 2010), and for many years, dihydroceramide was assumed to be inert, because treating cells with exogenous short-chain analogs did not cause noticeable defects (Hunot et al., 1997); hence, the potential physiological roles of dihydroceramide have been largely overlooked. In recent years, however, increased levels of dihydroceramide have been observed in the cerebrospinal fluid of Alzheimer's disease (AD) patients (Fonteh et al., 2015), and high levels of plasma dihydroceramide were found to predict AD-associated decline in cognitive function in a longitudinal study (Mielke et al., 2011). Altered levels of dihydrosphingolipids were also reported in a mouse model of Huntington's disease (Di Pardo et al., 2017). These findings inferred that the level of dihydroceramide may be important for neural function. In support of this idea, we previously showed that the *Drosophila* DEGS, *infertile crescent* (*ifc*), is required for neuronal maintenance, because neuron-specific knockout (KO) of *ifc* causes the accumulation of dihydroceramide and subsequent activity-dependent degeneration of photoreceptors (Jung et al., 2017). Notably, the defects in *ifc*-KO flies can be rescued by overexpression of a human homolog, *DEGS1*, suggesting functional conservation of fly and human enzymes. Furthermore, in 2019, three independent investigations found an association of *DEGS1* loss-of-function variants with leukodystrophy and systemic neuropathy (Dolgin et al., 2019; Karsai et al., 2019; Pant et al., 2019). Despite the clinical descriptions of patients and the phenotypic characterization of the fly model, the pathophysiological role of *DEGS1/ifc* and dihydroceramide in the nervous system remains poorly understood.

High levels of reactive oxygen species (ROS) are common to photoreceptors with *ifc*-KO and patient fibroblasts with *DEGS1* variants (Jung et al., 2017; Pant et al., 2019). Moreover, the elevated ROS in *ifc*-KO photoreceptors is known to cause morphological and functional defects that can be ameliorated by pan-antioxidant AD4 (Jung et al., 2017), but the mechanism underlying ROS accumulation has not been previously identified. Major sources of ROS include the mitochondrial electron transport chain, NADPH oxidases (NOXs), xanthine oxidases, peroxisomal

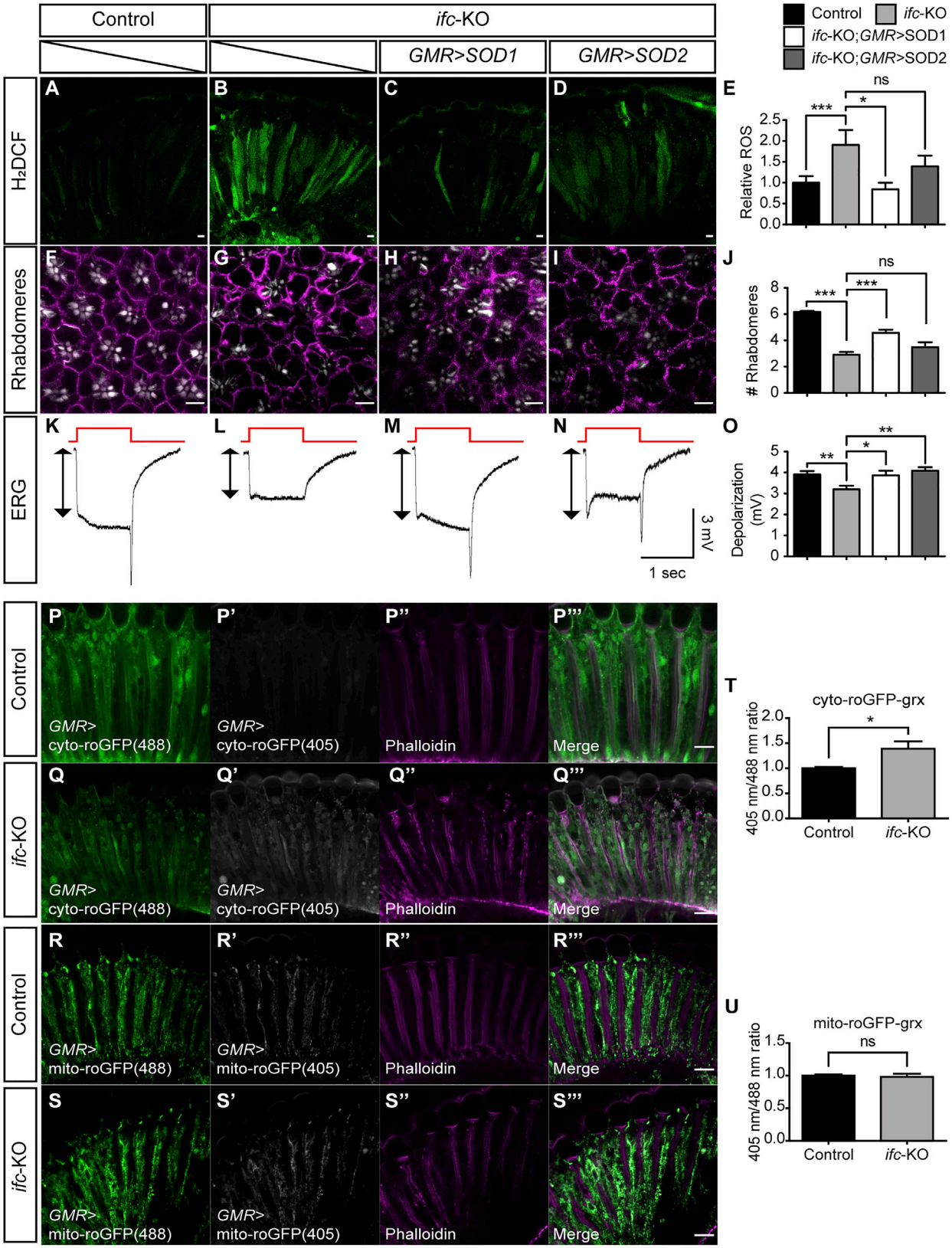

(legend on next page)

acyl-coenzyme A oxidase 1, and nitric oxide synthase (NOS), all of which have been linked to neuronal oxidative stress in different pathological contexts (Angelova and Abramov, 2018; Chung et al., 2020; Dawson and Dawson, 2018; Honorat et al., 2013; Sorce et al., 2017). Pan-antioxidant therapies have yielded promising results in preclinical models but did not show consistent positive effects in clinical trials. Instead, targeted antioxidants with subcellular precision might have better therapeutic potential. For instance, mitochondria-targeted antioxidants have shown protective effects in preclinical models and are in clinical trials to treat diseases manifesting mitochondrial oxidative stress (Snow et al., 2010; ClinicalTrials.gov: NCT00329056, NCT04267926, and NCT03514875). Therefore, identifying the subcellular sources of ROS in neurodegenerative conditions and the regulatory pathways that impinge upon those sources in neuronal cells may reveal future directions for potential therapeutics.

Proteins are often recruited to membrane rafts enriched in cholesterol and sphingolipids, in which they act as signaling molecules; these molecules may exhibit binding preferences for different organelles, depending on how the degree of lipid packing affects protein-membrane associations (Kulakowski et al., 2018; Resh, 2004). Both *ifc*-KO flies and *DEGS1*-compromised patient fibroblasts have lipid repertoires marked by increased dihydroceramide-to-ceramide ratios (Jung et al., 2017; Pant et al., 2019). Biophysical studies show that compared with ceramide-enriched membranes, dihydroceramide-enriched membranes are more condensed, contain fewer lipid-packing gaps, and associate more favorably with sphingomyelin, probably because of stronger intermolecular interactions (Kinoshita et al., 2020). Differences between dihydroceramide and ceramide in their intermolecular interactions with other lipids were proposed to affect the composition and packing of membrane rafts (Alanko et al., 2005). However, the potential effects of cellular dihydroceramide accumulation on the interactions between membranes and membrane-associated proteins have not been directly demonstrated.

Here, we found that dihydroceramide is a critical determinant of Rac1 compartmentalization and that loss of *ifc* causes neuronal (photoreceptor) defects by stimulating Rac1-NOX activation and cytoplasmic ROS accumulation. Importantly, the functional and morphological degeneration of *ifc*-KO eyes could be rescued by RNAi knockdown of Rac1/NOX or treatment of a NOX inhibitor. The cellular mechanisms that were identified in *ifc*-KO photoreceptors were also recapitulated in SH-SY5Y cells with the leukodystrophy-associated H132R variant of *DEGS1*; these cells exhibited accumulation of dihydroceramide, Rac1 activation, NOX-dependent cytoplasmic accumulation of ROS, and morphological defects. Colocalization and subcellular fractionation results revealed an increased level of Rac1 in the endolysosomes of *ifc*-KO photoreceptors and cells carrying homozygous H132R (*DEGS1*$^{H132R/H132R}$; hereafter called *DEGS1*^{H132R}) variants. According to liposome binding assays, excessive dihydroceramide can alter Rac1 association with membranes of different compartments, leading to Rac1 mislocalization. Altogether, the results of this study reveal a key molecular mechanism of dihydroceramide neurotoxicity and suggest an etiological role for the Rac1-NOX pathway in leukodystrophy arising from *DEGS1* variants.

RESULTS

Loss of *ifc* causes cytoplasmic ROS accumulation in fly photoreceptors

We previously reported that *ifc*-KO eyes exhibit ROS accumulation and subsequent neurodegeneration (Jung et al., 2017). To probe the subcellular origin of ROS in *ifc*-KO photoreceptors, we tested whether eye-specific, *GMR*-Gal4-driven overexpression of cytoplasmic and mitochondrial superoxide dismutases (SOD1 and SOD2, respectively) could protect against photoreceptor phenotypes. The level of ROS measured by H_2DCF staining was significantly decreased upon *GMR>SOD1* but not *GMR>SOD2* overexpression in *ifc*-KO photoreceptors (Figures 1A–1E), indicating that ROS was present mainly in the cytoplasm. Furthermore, overexpression of *SOD1* rescued the functional and morphological defects of *ifc*-KO eyes, as indicated by rhabdomere counts (Figures 1F–1J) and the electroretinography (ERG) measurement (Figures 1K–1O), respectively, suggesting that the cytoplasmic superoxide is the cause of photoreceptor dysfunction. Consistent with these findings, *GMR*-driven overexpression of *catalase*, which catalyzes the conversion of hydrogen peroxide to water and oxygen in cytoplasmic compartments, rescued photoreceptor degeneration (Figures S1A–S1H). The protective effects of SOD1 and catalase overexpression suggest that both superoxide and hydrogen peroxide played a pathogenic role in *ifc*-KO neurodegeneration. Although exogenous SOD2 expression did not ameliorate the accumulation of ROS (Figure 1D) or irregular morphology (Figure 1I), it did restore the function of *ifc*-KO photoreceptors (Figure 1N), implying that mitochondrial superoxide plays a minor role in *ifc*-KO neurodegeneration. To pinpoint the site of ROS genesis, we performed clonal analyses with a reduction-oxidation (redox)-sensitive GFP (roGFP) biosensor. Because the excitation peak of roGFP shifts from 488 to 405 nm upon oxidation of the protein, an

Figure 1. Cytoplasmic ROS accumulation in *ifc*-KO photoreceptors

(A–E) Photoreceptor longitudinal sections (A–D) stained with the ROS fluorescent probe H_2DCF (green) after 3 days of light exposure. The relative ROS levels are quantified in (E), with the intensity of control photoreceptors set to 1.

(F–J) Photoreceptor cross-sections (F–I) stained with phalloidin (white; rhabdomere) and Na^+-K^+-ATPase (purple; cell membrane) after 5 days of light exposure. The average number of rhabdomeres per ommatidia is quantified in (J).

(K–O) Representative ERG traces (K–N) of flies upon light stimulation. Double-ended arrows indicate depolarization. Flies were exposed to light for 5 days before ERG recordings. The average depolarization amplitudes (in millivolts) of adult fly eyes are quantified in (O).

(P–U) Photoreceptor longitudinal sections of control (P–P‴) and *ifc*-KO (Q–Q‴) photoreceptors with GMR-driven overexpression of cyto-roGFP-grx. The 405/488-nm ratios of cyto-roGFP are quantified in (T). Photoreceptor longitudinal sections of control (R–R‴) and *ifc*-KO (S–S‴) photoreceptors with GMR-driven overexpression of mito-roGFP-grx. The 405/488-nm ratios of mito-roGFP are quantified in (U).

The genotype of each group is listed in method details. Scale bars: 5 μm. Error bars represent SEM; n ≥ 5 for each experiment with ≥3 independent experiments. *p < 0.05, **p < 0.01, ***p < 0.001, unpaired Student's t test.

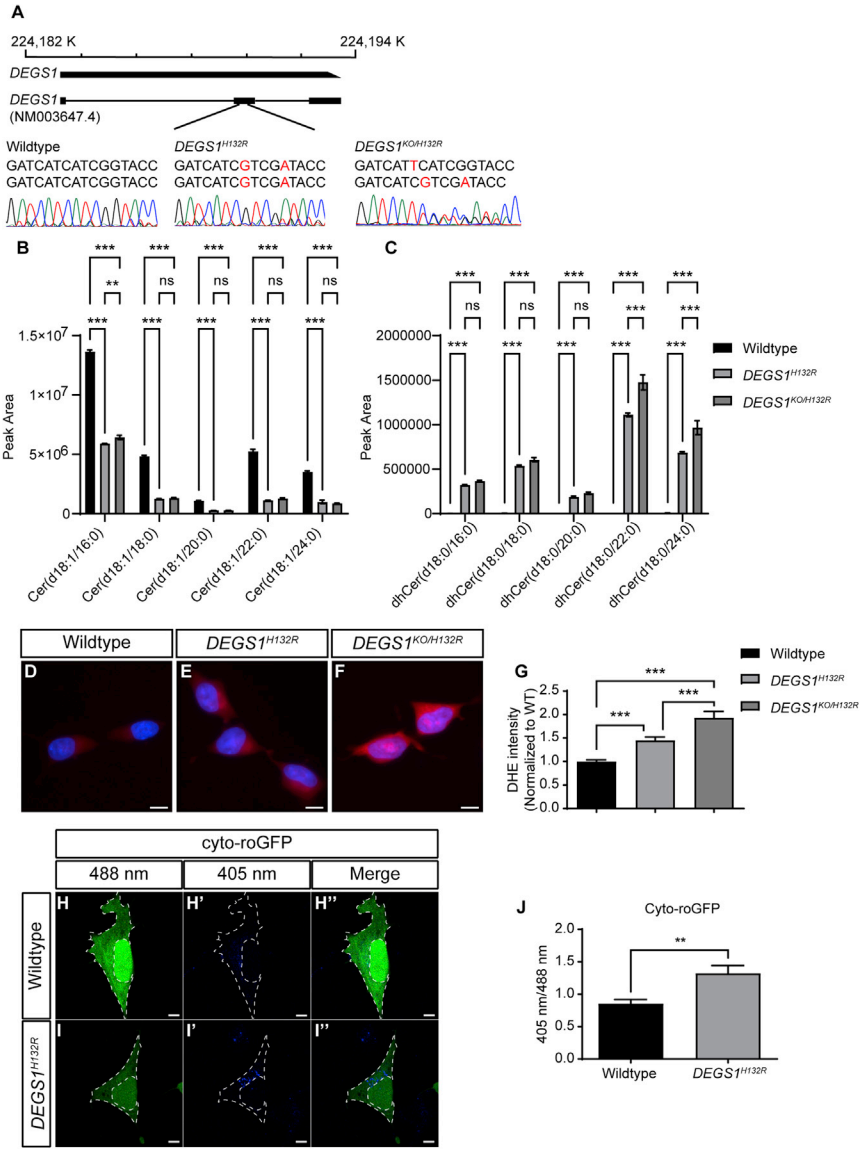

Figure 2. Dihydroceramide and cytoplasmic ROS accumulations in *DEGS1*^{H132R} SH-SY5Y neuroblastoma cells

(A) Schematic of *DEGS1*^{H132R} CRISPR knockin.

(B) Ceramide levels of wild-type, *DEGS1*^{H132R}, and *DEGS1*$^{KO/H132R}$ SH-SY5Y cells measured by HPLC-MS/MS.

(C) Dihydroceramide levels of wild-type, *DEGS1*^{H132R}, and *DEGS1*$^{KO/H132R}$ SH-SY5Y cells measured by HPLC-MS/MS.

(D–G) ROS detected in wild-type, *DEGS1*^{H132R}, and *DEGS1*$^{KO/H132R}$ SH-SY5Y cells with the fluorescent probe dihydroethidium (DHE). The intensity of DHE is quantified in (L), with the intensity of wild-type cells set to 1.

(H–J) Wild-type (H–H‴) and *DEGS1*^{H132R} (I–I‴) SH-SY5Y cells expressing cyto-roGFP. The 405/488-nm ratio of cyto-roGFP in SH-SY5Y cells is quantified in (J). The nucleus was excluded from the quantification. The region of interest is encircled by a dashed line.

Scale bars: 5 μm. Error bars represent SEM; n ≥ 3 independent experiments. *p < 0.05, **p < 0.01, ***p < 0.001, unpaired Student's t test.

increased ratio of the 405-nm-excited to the 488-nm-excited roGFP signal is indicative of ROS elevation. We used roGFP targeted to the cytoplasm (*GMR* > cyto-roGFP-grx) and mitochondrial matrix (*GMR* > mito-roGFP-grx) as compartment-specific ROS probes in *ifc*-KO eyes (Albrecht et al., 2011). The mitochondrial localization of mito-roGFP in photoreceptors was confirmed by staining for ATP5A (Figure S1K). The 405/488-nm ratio of cyto-roGFP was significantly increased in *ifc*-KO photoreceptors compared with controls (Figures 1P–1Q and 1T), whereas the ratio for mito-roGFP was similar to the control value (Figures 1R, 1S, and 1U). In mosaic eye clones, we also found that the *ifc*-KO cells exhibited lower cyto-roGFP intensities than wild-type sister clones labeled with red fluorescent protein (RFP) (Figure S1I). In contrast, no differences in the intensities of mito-roGFP were observed between *ifc*-KO and control photoreceptors (Figure S1J). Altogether, these results suggested that ROS in the cytoplasm is responsible for causing the neuronal defects in *ifc*-KO photoreceptors.

Accumulation of cytoplasmic ROS in *DEGS1*^{H132R} SH-SY5Y cells

The H132R variant of human *DEGS1* is associated with an autosomal recessive form of leukodystrophy (Pant et al., 2019). In this variant, an amino acid substitution of conserved histidine to arginine within one of the putative catalytic motifs critically compromises ceramide synthesis. To explore the pathogenic cellular mechanisms induced by the H132R variant, we introduced it into SH-SY5Y neuroblastoma cells by CRISPR/Cas9 knockin (Figure 2A). Our sphingolipidomics analyses revealed that cells carrying either *DEGS1*^{H132R} or compound heterozygous H132R (*DEGS1*$^{KO/H132R}$) variants had significant reductions in ceramide levels and accumulation of dihydroceramide (Figures 2B and 2C), indicating the H132R variant is a loss-of-function allele. In addition, the neurite lengths of *DEGS1*^{H132R} and *DEGS1*$^{KO/H132R}$ SH-SY5Y cells were significantly shorter than those in wild-type cells, indicating a morphological defect (Figures S2A–S2D). To test whether the H132R variant in SH-SY5Y cells recapitulated the ROS accumulation in *ifc*-KO photoreceptors and *DEGS1*-deficient patient fibroblasts (Pant et al., 2019), we measured ROS levels using dihydroethidium (DHE), which detects superoxide. The DHE intensities in *DEGS1*^{H132R} and *DEGS1*$^{KO/H132R}$ cells were significantly higher than that in control cells (Figures 2D–2G). Similarly, small interfering RNA (siRNA) knockdown of *DEGS1* led to reduced neurite length (Figures S2H–S2K) and increased DHE intensity

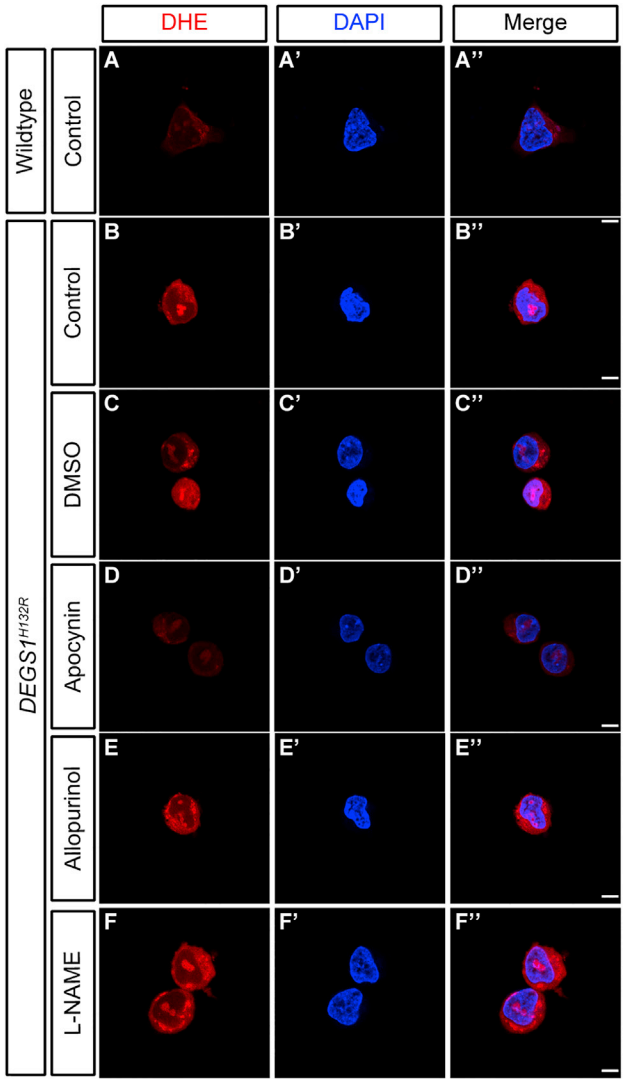

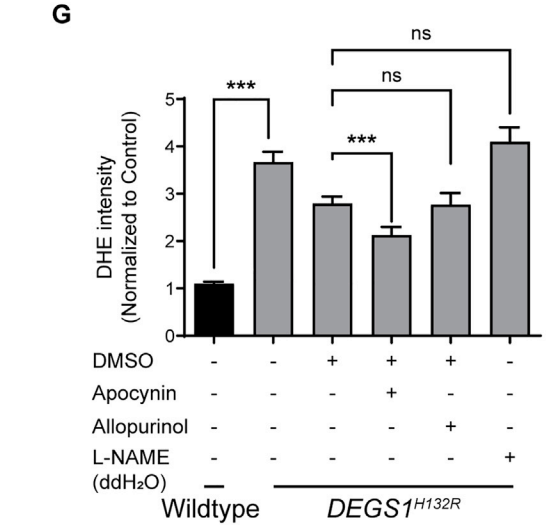

Figure 3. Identification of the major origins of ROS in *DEGS1*^{H132R} cells

(A–F) DHE staining in wild-type (A–A′′) and *DEGS1*^{H132R} (B–B′′) SH-SY5Y cells. *DEGS1*^{H132R} cells were treated with DMSO (C–C′′) (vehicle control), apocynin (D–D′′) (50 μM; NADPH oxidase inhibitor), allopurinol (E–E′′) (100 μM; xanthine oxidase inhibitor), and L-NAME (F–F′′) (50 μM; nitric oxide synthase inhibitor). (G) Quantification of the intensity of DHE in SH-SY5Y cells, with the intensity of wild-type cells set to 1.

Scale bars: 5 μm. Error bars represent SEM; n ≥ 3 independent experiments. *p < 0.05, **p < 0.01, ***p < 0.001, one-way ANOVA with multiple comparisons using Tukey post hoc test.

(Figures S2L–S2O). In contrast, the intensity of a mitochondrial superoxide probe, MitoSOX, was not increased in *DEGS1*^{H132R} cells compared with wild-type cells (Figures S2E–S2G). To evaluate the level of hydrogen peroxide production, we measured the extracellular level of hydrogen peroxide by the Amplex red-horseradish peroxidase (HRP) assay and found that the levels were not different in wild-type, *DEGS1*^{H132R}, and *DEGS1*$^{KO/H132R}$ cells (Figure S2P). Because we saw that loss of *ifc* induced cytoplasmic ROS accumulation, we next transfected cyto-roGFP into wild-type and *DEGS1*^{H132R} cells and examined the redox state in the cytoplasm. Consistent with our findings in *ifc*-KO photoreceptors, the 405/488-nm ratio of cyto-roGFP was significantly increased in *DEGS1*^{H132R} compared with wild-type SH-SY5Y cells (Figures 2H–2J). These data showed that the disease-associated H132R variant of *DEGS1* and KO of *ifc* lead to similar cellular defects, including an imbalance of dihydroceramide and ceramide, cytoplasmic ROS accumulation, and morphological defects. Thus, defects in the *DEGS1/ifc* genes are likely to affect neurons in flies and humans via a conserved mechanism.

NOX inhibitors alleviate oxidative stress in *DEGS1*^{H132R} neuroblastoma cells

Different types of cytoplasmic ROS are frequently produced by enzymes such as NOXs, xanthine oxidase, or uncoupled NOS. To test whether any of these enzymes is responsible for the ROS accumulation in *DEGS1*^{H132R} cells, we suppressed the activity of each by chemical inhibition and examined the subsequent levels of ROS by DHE staining (Figure 3). The high cytoplasmic ROS level in *DEGS1*^{H132R} cells was ameliorated by the treatment of the NOX inhibitor apocynin (Figures 3D–3D′), but not the xanthine oxidase inhibitor allopurinol (Figures 3E–3E′) or the NOS inhibitor L-NAME (Figures 3F–3F′). We verified this result with a highly specific NOX inhibitor, GKT136901, which has no ROS scavenging effect and does not inhibit other oxidases (Laleu et al., 2010). GKT136901 treatment reduced the superoxide level of *DEGS1*^{H132R} cells compared with the vehicle control (Figure S3). These results suggest that NOX complexes are the major source of ROS in *DEGS1*^{H132R} cells.

Activation of the Rac1-NOX pathway causes oxidative stress and subsequent neurodegeneration in *ifc*-KO photoreceptors

Because the small guanosine triphosphatase (GTPase) Rac1 is a cytosolic protein required for NOX activation, we examined its role in *ifc*-KO photoreceptors. We first found that the level of Rac1 protein was increased in *ifc*-KO eyes compared with

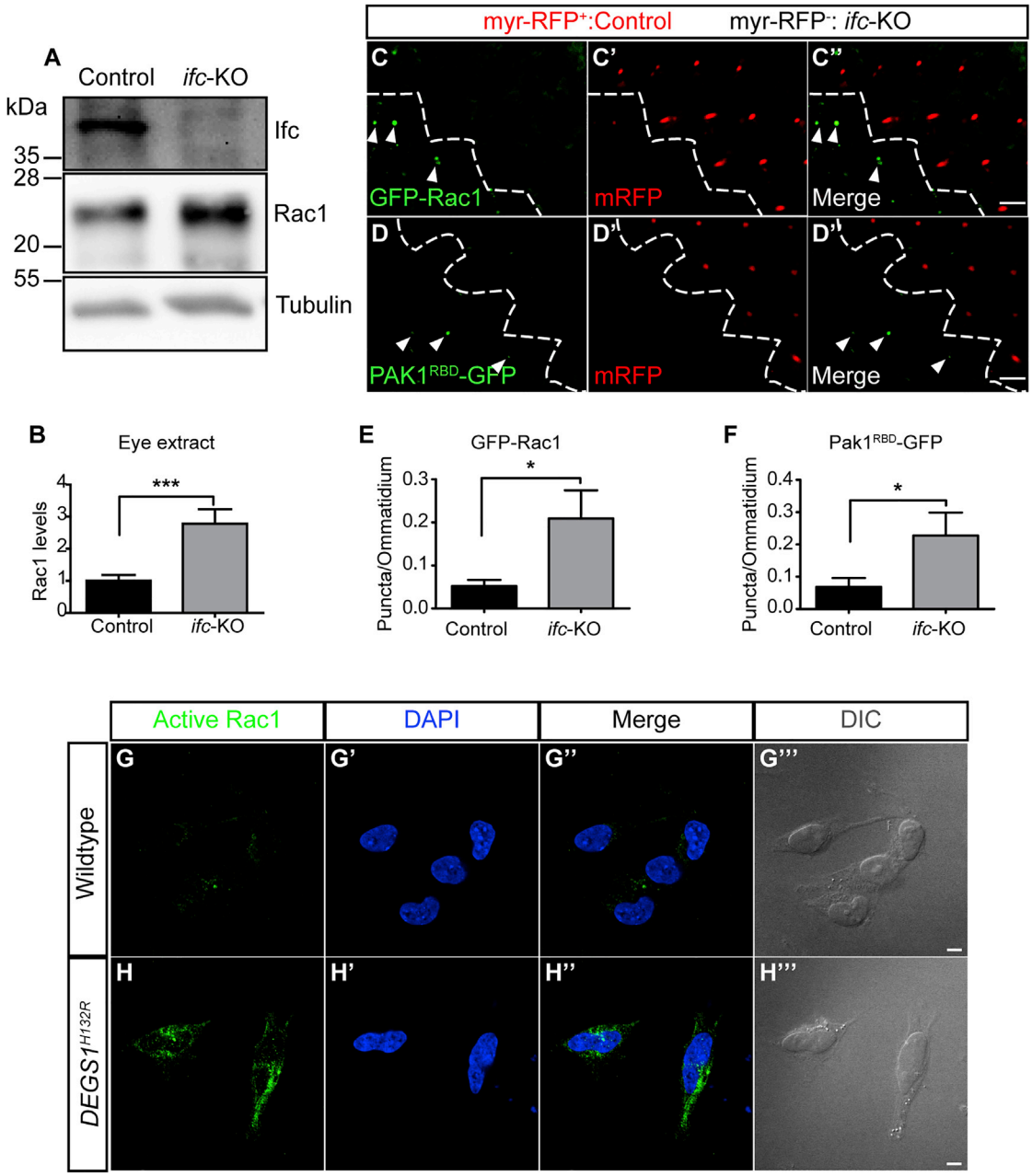

Figure 4. Activation of Rac1 signaling in both fly *ifc*-KO photoreceptors and SH-SY5Y *DEGS1*^{H132R} cells

(A and B) Western blot of Rac1 comparing the eye extracts of control and *ifc*-KO. The levels of Rac1 (normalized to tubulin) in eye extracts are quantified in (B).

(C–F) Cross-section images of *ifc*-KO mosaic eye clone with endogenous expression of GFP-Rac1 (C) or PAK1^{RBD}-GFP (D). Control photoreceptors were marked with GMR-myr-RFP (C′ and D′), separated by a dashed line from *ifc*-KO photoreceptors lacking RFP signals. Arrowheads indicate the puncta of GFP-Rac1 or PAK1^{RBD}-GFP. The average numbers of GFP-Rac1 or PAK1^{RBD}-GFP puncta per ommatidia are quantified in (E) and (F).

(G and H) Immunostaining with anti-active Rac1 antibody (green) in wild-type (G) and *DEGS1*^{H132R} (H) SH-SY5Y cells.

Scale bars: 5 μm. Error bars represent SEM; n ≥ 3 independent experiments. *p < 0.05, **p < 0.01, ***p < 0.001, unpaired Student's t test.

controls (Figures 4A and 4B). Then, we again took advantage of fly genetics tools, comparing the activities of Rac1 in *ifc*-KO mosaic eye clones with two GFP reporters. When GFP-tagged Rac1 was expressed under the control of endogenous Rac1 regulatory elements (Abreu-Blanco et al., 2014), the numbers of GFP-Rac1 puncta were significantly increased in the mutant clones compared with adjacent wild-type clones, indicating an increased level of Rac1 protein (Figures 4C and 4E). Next, to measure the activity of Rac1 in photoreceptors, we used the Pak1^{RBD}-GFP construct, a ubiquitously expressed reporter for the association of Rac1 to Pak1, which is a downstream effector of Rac1 (Arbeu-Blanco et al., 2014). The numbers of

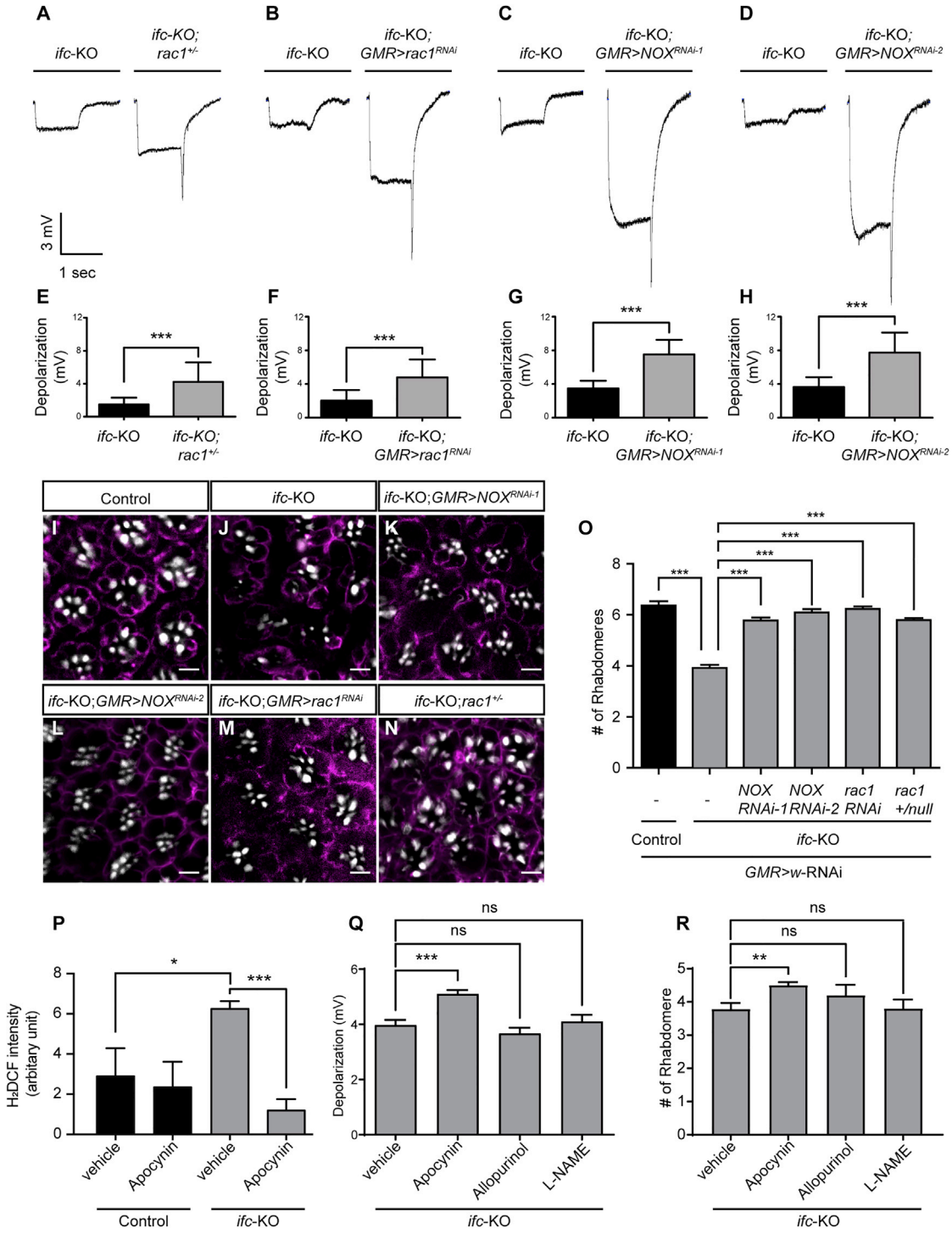

Figure 5. Amelioration of *ifc*-KO neuronal defects via genetic and pharmacological inhibition of the Rac1-NOX pathway

(A–H) Representative ERG traces upon light stimulation in *ifc*-KO eyes with *rac1* heterozygote (A, BL6647), *rac1 RNAi* knockdown (B, BL28985), and *NOX RNAi* knockdown (C, BL32902; D, BL32433) backgrounds after 5 days of light exposure. The upstream activating sequence (UAS)-*RNAi* was driven by eye-specific *GMR*-Gal4. The average depolarization amplitude (in millivolts) of ERG is quantified in (E)–(H).

(I–O) Photoreceptor cross-sections (I–N) stained with phalloidin (white; rhabdomere) and Na^+-K^+-ATPase (purple; cell membrane) after 5 days of light exposure. The average number of rhabdomeres per ommatidia is quantified in (O).

(P) Quantification of H_2DCF staining of control and *ifc*-KO photoreceptors with vehicle (DMSO) and apocynin treatment. Representative figures are shown in Figures S4A–S4D.

(legend continued on next page)

Pak1^{RBD}-GFP puncta were increased in *ifc*-KO photoreceptors compared with adjacent control clones (Figures 4D and 4F), indicating activation of the Rac1 pathway. Likewise, in *DEGS1*^{H132R} SH-SY5Y cells, we observed an increased immunofluorescence signal for active Rac1 compared with wild type when probing with an antibody that preferentially recognizes guanosine triphosphate (GTP)-bound, active Rac1 (Figures 4G and 4H). These results all support the idea that loss of *DEGS1/ifc* increases the Rac1 protein level and activates Rac1.

Next, to test whether the activation of Rac1-NOX signaling is required for degeneration in *DEGS1/ifc*-deficient conditions, we genetically suppressed the Rac1-NOX pathway in *rac1* heterozygotes and flies with *GMR*-Gal4-driven RNAi knockdown of *rac1* and *NOX* in *ifc*-KO photoreceptors. These genetic means of inhibiting the Rac1-NOX pathway significantly alleviated the functional and morphological degeneration of *ifc*-KO photoreceptors (Figures 5A–5O). Next, we compared the effects of inhibitors of ROS production on the degeneration of *ifc*-KO photoreceptors (Figure S4). Apocynin significantly reduced the ROS levels (Figure 5P) and improved the function and morphology of *ifc*-KO photoreceptors, whereas allopurinol and L-NAME did not provide significant protection (Figures 5Q and 5R). These observations were consistent with the effects of the inhibitors in *DEGS1*^{H132R} cells (Figure 3). Altogether, these results indicate that activation of the Rac1-NOX complex is responsible for the ROS-induced degeneration of *ifc*-KO photoreceptors.

Loss of *ifc* promotes colocalization of active Rac1 and Rab7-positive compartments

We then asked how *ifc* regulates the Rac1 pathway. Because Rac1 compartmentalization has been shown to play a crucial role in downstream signaling (Payapilly and Malliri, 2018), we examined whether *ifc* might affect subcellular localization of active Rac1. To do so, we performed costaining with the active Rac1-specific antibody and markers of various subcellular compartments (Figures 6A–6J″). The percentages of colocalized puncta (arrowhead) among total active Rac1 puncta were quantified for each compartment (Figures 6K–6O). Intriguingly, the colocalization of active Rac1 and the late endosome/lysosome marker Rab7 was significantly increased in *ifc*-KO photoreceptors compared with controls (Figures 6E–6F″and 6M). In contrast, *ifc*-KO did not affect the colocalization between active Rac1 and markers of early endosomes (Rab5; Figures 6I–6J″and 6O), mitochondria (TOM20; Figures 6C–6D″and 6L), autophagosomes (GABARAP; Figures 6G–6H″and 6N), or endoplasmic reticulum (ER) (BIP; Figures 6A–6B″and 6K). To test whether the effect of *DEGS1/Ifc* deficiency on Rac1 localization was conserved between fly and human, we performed subcellular fractionation of wild-type and *DEGS1*^{H132R} cells to examine the subcellular distribution of Rac1 protein. In both cell lines, Rac1 protein was found primarily in the cytosolic, endosomal, and ER/plasmalemma fractions (Figure S5). We quantified the level of Rac1 in distinct subcellular compartments and found significantly increased levels of Rac1 in Rab7-enriched compartments of *DEGS1*^{H132R} cells compared with controls (Figures 6P and 6Q). Altogether, these data show that both the loss of *ifc* in fly photoreceptors and the H132R variant of *DEGS1* in SH-SY5Y cells cause mislocalization of Rac1 to endolysosomes.

Dihydroceramide levels determine Rac1 association with reconstituted plasma membrane rafts and autophagosomes

Localized Rac1 signaling starts with the binding of active Rac1 to the membrane of a distinct subcellular compartment (Payapilly and Malliri, 2018). Because Ifc converts dihydroceramide to ceramide and its absence affects the subcellular localization of active Rac1 (Figure 6), we hypothesized that these two sphingolipids modulate the membrane association of Rac1. To test the hypothesis, we first measured the levels of ceramide and dihydroceramide in distinct subcellular compartments of wild-type and *DEGS1*^{H132R} cells by high-performance liquid chromatography-tandem mass spectrometry (HPLC-MS/MS) following subcellular fractionation. We observed increases of dihydroceramide and decreases of ceramide content in all examined subcellular compartments, including cytosol, late endosomes, ER/plasmalemma, and mitochondria (Figure S6). Next, to test whether dihydroceramide and ceramide content can mediate Rac1 membrane binding, we performed a liposome binding assay using large unilamellar vesicles (LUVs) that mimic subcellular membranes (Figures 7A–7F). Plasma membrane rafts are well-known sites of Rac1 binding; thus, we composed LUVs with lipid compositions that mimic that of membrane rafts (del Pozo et al., 2004) (Figures 7A–7C). The presence of dihydroceramide reduced the association of GTP-Rac1 (active) (Figure 7B). Next, because dihydroceramide accumulation has been shown to induce autophagy and we previously reported the activation of protective autophagy in *ifc*-KO photoreceptors (Jung et al., 2017), we tested how dihydroceramide and ceramide affect the binding of Rac1 to autophagosome-like liposomes (Rao et al., 2016) (Figures 7D–7F). Increasing the dihydroceramide content in autophagosome-like liposomes improved the membrane binding of active Rac1 (Figure 7E). In contrast, changing ceramide levels did not significantly affect the association of Rac1 to LUVs, highlighting that altering the interaction between Rac1 and membranes is a distinct biochemical property of dihydroceramide. To elucidate whether the association between Rac1 and membrane rafts is disturbed in *DEGS1*-compromised cells, we compared the level of Rac1 in a detergent-resistant membrane raft fraction from wild-type and *DEGS1*^{H132R} cells (Figure 7G; Figures S7A and S7B). The level of Rac1 associated with membrane rafts of *DEGS1*^{H132R} cells was significantly lower than that of wild-type cells (Figure 7H). This observation was consistent with the result of our liposome binding assay,

(Q) Quantification of ERG depolarization of *ifc*-KO photoreceptors with vehicle, apocynin, allopurinol, and L-NAME treatments. Representative figures are shown in Figures S4J–S4O.

(R) Quantification of the average number of rhabdomeres per ommatidia of *ifc*-KO photoreceptors with vehicle, apocynin, allopurinol, and L-NAME treatments. Representative figures are shown in Figures S4E–S4I.

Scale bars: 5 μm. Error bars represent SEM; n ≥ 3 independent experiments. *p < 0.05, **p < 0.01, ***p < 0.001, unpaired Student's t test.

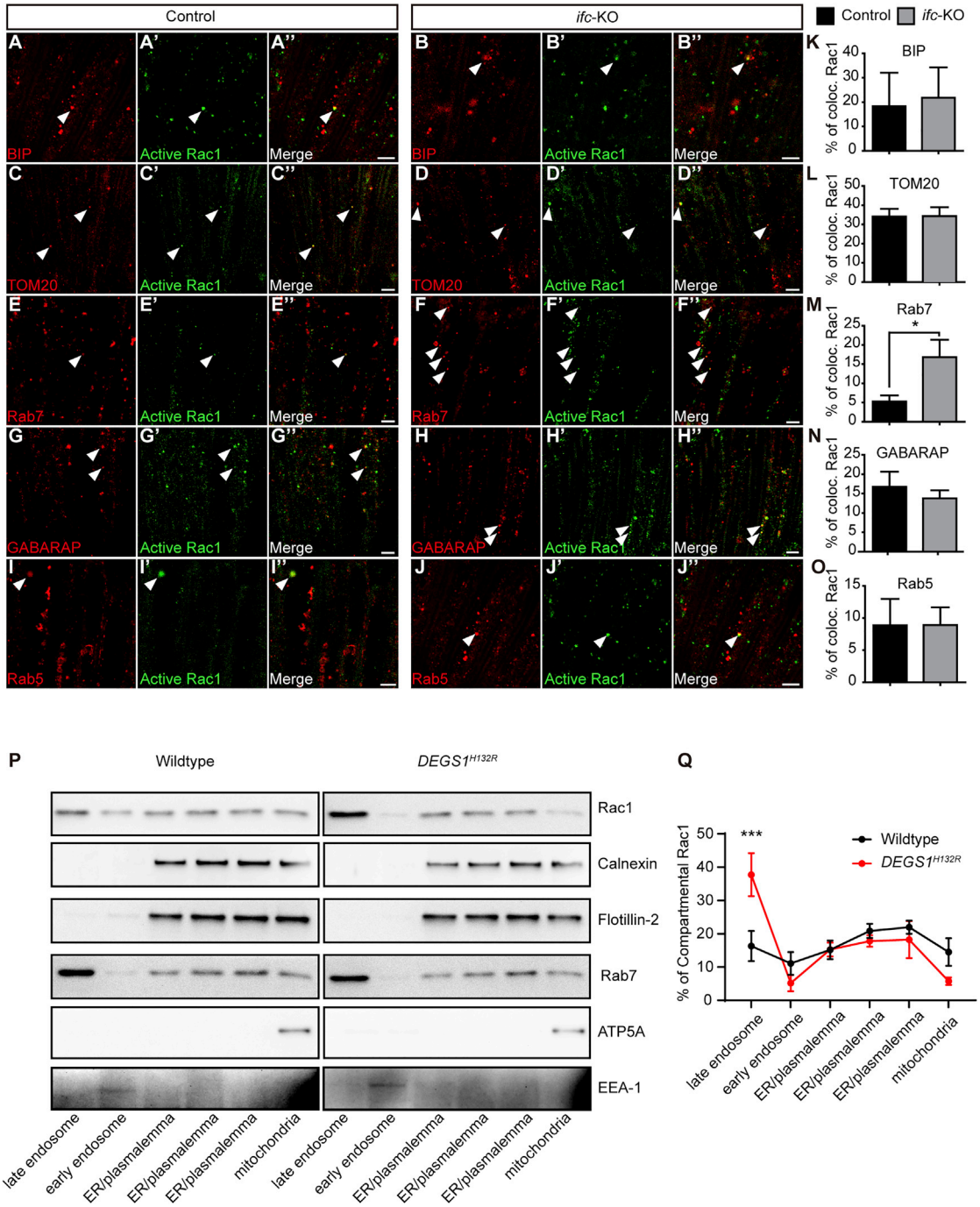

Figure 6. Increased subcellular colocalization of GTP-Rac1 and Rab7 in *ifc*-KO photoreceptors

(A–O) Colocalization of active Rac1 (green) and markers of various subcellular compartments (red), including BIP (A–B′) (ER lumen), TOM20 (C–D′) (mitochondrial outer membrane), Rab7 (E–F′) (endolysosome), GABARAP (G–H′) (autophagosome), and Rab5 (I–J′) (early endosome), in fly photoreceptor longitudinal sections. Arrowheads indicate the colocalized puncta between GTP-Rac1 and compartmental markers. The percentages of active Rac1 puncta colocalizing with compartmental markers in total numbers of active Rac1 puncta are quantified in (K)–(O).

(P and Q) Western blot of Rac1 and compartmental markers including calnexin (ER membrane), ATP5A (mitochondria), flotillin-2 (lipid raft), and EEA-1 (early endosome) of wild-type and *DEGS1*^{H132R} SH-SY5Y cells. The percentage of compartmentalized Rac1 levels is quantified in (Q).

Scale bars: 5 μm. Error bars represent SEM; n ≥ 3 independent experiments. *p < 0.05, **p < 0.01, ***p < 0.001, unpaired Student's t test (O and P) or two-way ANOVA with multiple comparison using the Šídák test.

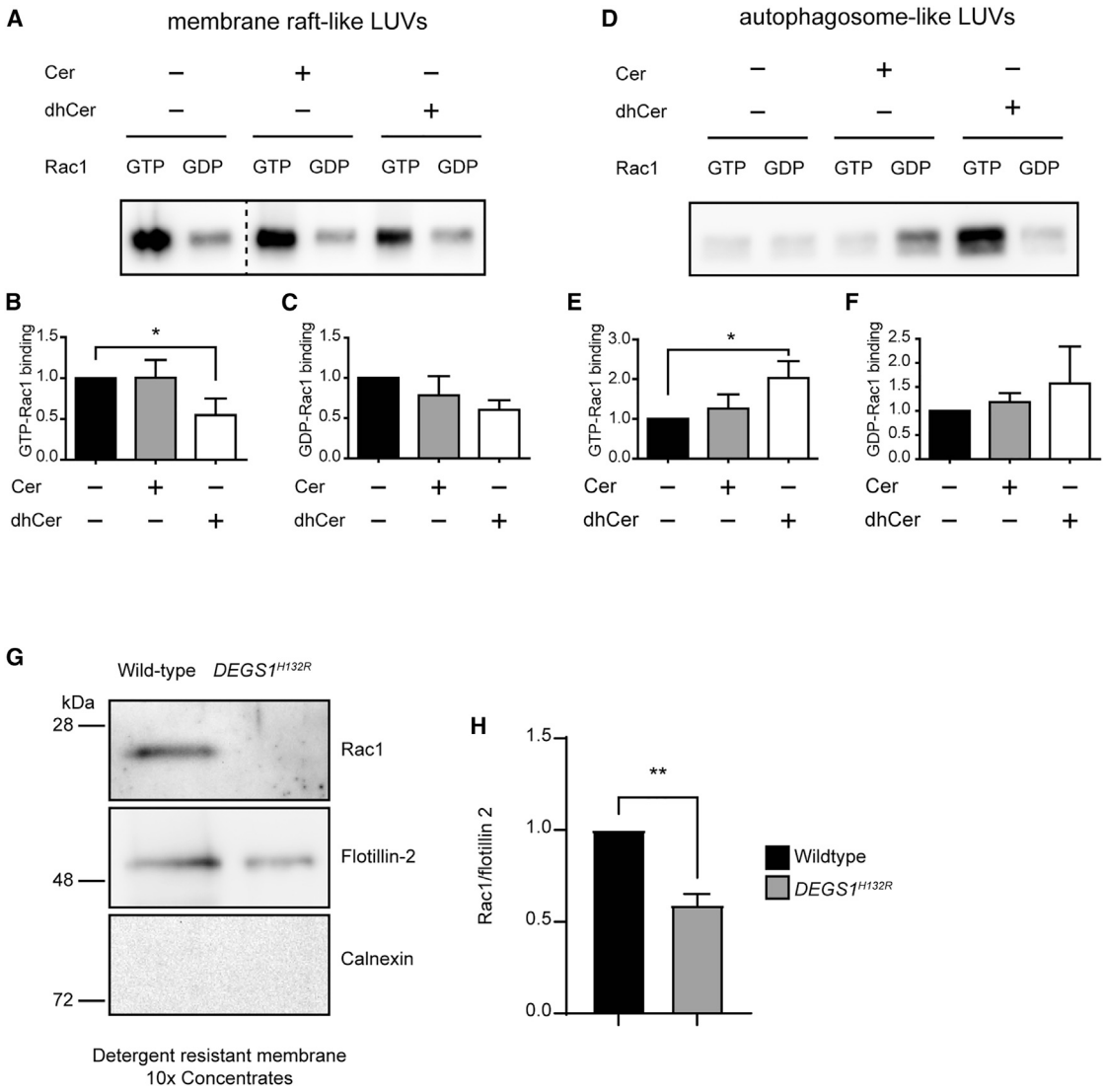

Figure 7. The effect of dihydroceramide on the binding of Rac1 to liposomes mimicking distinct subcellular compartments

(A–C) Western blot of Rac1 associated with membrane raft-like liposomes. The levels of GTP-Rac1 and guanosine diphosphate (GDP)-Rac1 associated with membrane raft-like liposomes are quantified in (B) and (C), respectively. The lanes separated by the dashed line were run on the same blot.

(D–F) Western blot of Rac1 associated with autophagosome-like liposomes. The levels of GTP-Rac1 and GDP-Rac1 associated with autophagosome-like liposomes are quantified in (E) and (F), respectively.

(G and H) Western blot of Rac1 and flotillin-2 in detergent-resistant membrane fractions of wild-type and *DEGS1*^{H132R} SH-SY5Y cells. The level of Rac1 normalized to flotillin-2 is quantified in (H).

Error bars represent SEM; n ≥ 3 independent experiments. *p < 0.05, **p < 0.01, ***p < 0.001, unpaired Student's t test.

suggesting low binding between Rac1 and dihydroceramide-rich membrane rafts. We also examined whether altered levels of raft-localized Rac1 affect ROS production on the plasma membrane by adding a CAAX motif to the C terminus of roGFP. The CAAX motif is a prenylation site that allows plasma membrane binding. The 405/488-nm ratio of roGFP-CAAX was not different in wild-type and *DEGS1*^{H132R} cells (Figures S7C–S7E), ruling out the plasma membrane as a major source of ROS. Thus, we suspect that dihydroceramide accumulation creates a hub for ROS accumulation within the cell cytoplasm, given the increase in cytoplasmic ROS (Figure 1) and endolysosomal Rac1 activation (Figure 6). These data reveal a role for dihydroceramide in modulating the membrane association of Rac1.

DISCUSSION

In the present study, we determined the subcellular origin and the molecular mechanism of ROS production in *ifc*-KO photoreceptors and leukodystrophy-associated *DEGS1*^{H132R} SH-SY5Y cells. We found that the loss of *ifc* and the *H132R* variant of *DEGS1* both caused the mislocalization of Rac1 to Rab7-

positive compartments, i.e., endolysosomes and autolysosomes. This mislocalization likely results from the effects of accumulated dihydroceramide on the membrane association of Rac1, which is pivotal to Rac1 function. Importantly, genetic and pharmacological inhibition of the Rac1-NOX pathway reduced the level of ROS and rescued the morphological and functional degeneration of *ifc*-KO photoreceptors. Altogether, these experimental results support the idea that DEGS activity is required for proper compartmentalization of Rac1 and neuronal maintenance.

A growing body of literature has begun to describe distinct features and pathophysiological roles of dihydroceramide that are independent of ceramide (reviewed in Rodriguez-Cuenca et al., 2015; Siddique et al., 2015). However, with regard to neuronal oxidative stress, no previous research reports have addressed how dihydroceramide accumulation might elevate ROS levels and cause neuronal defects. Still, increased ceramide has been shown to cause apoptosis through mitochondrial oxidative stress in neuroblastoma cells (Czubowicz and Strosznajder, 2014), and exogenous ceramide was shown to decrease mitochondrial membrane potential in cultured retinal neurons (Prado Spalm et al., 2019). In addition, oxidative stress from tumor necrosis factor alpha (TNF-α)-induced ceramide production in SH-SY5Y cells could be mitigated by NOX inhibition (Barth et al., 2012). Although these studies showed that ceramide species were cytotoxic, the application of those findings may be limited, because the studies were performed by adding exogenous short-chain ceramides to cultured neurons and did not address the long-overlooked, less studied dihydroceramide. To understand the biological effects of endogenous dihydroceramide, we previously knocked out *ifc*, the key gene regulating *de novo* ceramide synthesis, and by doing so, we found that the neurotoxicity results from ROS accumulation (Jung et al., 2017). In this study, we extend this observation to unveil a conserved molecular mechanism in which dihydroceramide regulates the site of Rac1-NOX activation by affecting the association of active Rac1 to biological membranes.

The multi-functionality of Rac1 primarily depends on its compartmentalization (Payapilly and Malliri, 2018). One important factor that controls the association of Rac1 to specific subcellular sites is the lipid composition of membranes. For instance, different phospholipids have been shown to modulate the recruitment of Rac1 to microdomains on the plasma membrane (Magalhaes and Glogauer, 2010). Although sphingolipids are major constituents of membrane microdomains, the impacts of sphingolipid content on the sites of Rac1 action were unknown. Our study shows dihydroceramide is a critical determinant of the binding between active Rac1 and membranes. In addition to regulating Rac1 compartmentalization, ceramides and ceramide-enriched membrane domains have been shown to modulate the subcellular localization and responses of a spectrum of proteins by direct effects on binding or by altering membrane properties (Fekry et al., 2018; Grassmé et al., 2001; Kajimoto et al., 2004; Zhu et al., 2019). Therefore, *DEGS1*/*ifc* deficiency and the consequent changes in relative levels of ceramide and dihydroceramide may broadly affect subcellular signaling in the context of neurodegeneration and beyond.

Our results suggest that sphingolipid imbalance, especially in the dihydroceramide-to-ceramide ratio, may cause neuronal defects by altering membrane association of signaling molecules. Aside from *DEGS1*, other mutations in genes of the ceramide *de novo* synthesis pathway (including *SPTLC1*, *SPTLC2*, *CERS1*, and *CERS2*) have been clinically associated with neural disorders (Bejaoui et al., 2001; Dawkins et al., 2001; Godeiro Junior et al., 2018; Karsai et al., 2019; Mosbech et al., 2014; Pant et al., 2019; Rotthier et al., 2010; Vanni et al., 2014). Nevertheless, mechanistic investigations into the specific neuronal defects in these disorders are only in beginning stages. In animal models of hereditary sensory and autonomic neuropathy type 1 (HSAN1), ectopic expression of dominant-negative variants of the *Drosophila* and *C. elegans Spt1* gene caused dysregulated vesicle trafficking (Cui et al., 2019; Oswald et al., 2015). In addition, a mouse model of HSAN1 with ablation of *Sptlc2* manifested significant ER stress and prolonged activation of mTORC1 (Wu et al., 2019). Downstream of *SPTLC1/2*, deficiencies in ceramide synthase 1 and 2 caused progressive myoclonic epilepsy (Godeiro Junior et al., 2018; Mosbech et al., 2014; Vanni et al., 2014). In astrocyte cultures from *CerS2* null mice, altered ceramide compositions induced mitochondrial oxidative stress and impaired clathrin-mediated endocytosis (Volpert et al., 2017). Because mutations of genes in the *de novo* pathway cause obvious alterations in the sphingolipid profile, the confirmed pathological roles of imbalanced sphingolipids warrant a series of detailed investigations. In line with this goal, our findings provide an interesting and important example of how a specific sphingolipid species, dihydroceramide, participates in the pathogenesis of neural disorders.

One caveat of the present study is that because of technical limitations, we were unable to determine whether the effects in *DEGS1*/*ifc*-deficient neurons were caused by an overall increase in the Rac1 protein level or mislocalization of active Rac1 to endolysosomes. Indeed, an overall increase of the Rac1 protein level in *ifc*-KO and *DEGS1*^{H132R} cells may promote NOX activation. Although we showed that dihydroceramide reduces the association of active Rac1 to membrane rafts, we did not detect a decrease in the ROS level at the plasma membrane (Figures S7C–S7E). However, we observed a significant increase of active Rac1 in the Rab7-positive compartment and cytoplasmic ROS accumulation in *ifc*-KO photoreceptors and *DEGS1*^{H132R} cells (Figure 6), suggesting Rac1-NOX was activated in the endolysosomal compartment. Unfortunately, we could not directly measure whether the accumulation of active Rac1 leads to the activation of NOX in the endolysosomal compartment to produce ROS. Further technical advances will be needed to evaluate the activation of NOX in specific subcellular compartments.

Another limitation of the present study is that the exact type of ROS mechanistically linked to the *DEGS1*/*ifc*-associated neurodegeneration was not defined. We showed that genetic and chemical inhibition of NOX rescued *ifc*-KO neurodegeneration, suggesting a pathogenic role for superoxide. In addition, overexpression of SOD1 and catalase rescued the neuronal defects of *ifc*-KO photoreceptors, indicating that superoxide and hydrogen peroxide also participate in the pathogenesis. Although we found no difference in extracellular hydrogen peroxide levels between wild-type and *DEGS1* mutant cells using the Amplex red-

HRP assay, other methods, such as a hyperfluorescent probe for detecting intracellular hydrogen peroxide or treatment with catalase mimetics, should be exploited to better evaluate the roles of different ROS types. Because hydrogen peroxide and hydroxyl radicals can be derived from superoxide, it is possible that superoxide generated via the NOX-dependent pathway subsequently leads to an overall increase in different types of ROS in the cytoplasm. Our findings revealed that dihydroceramide accumulation in SH-SY5Y and *Drosophila* neurons activates Rac1-NOX-mediated production of ROS and points to antioxidant defense as a potential therapeutic approach. Identification of the specific types of ROS in the pathogenic mechanism may provide insights into the development of precise treatment strategies and thus warrants future studies.

In the present report, we introduce the concept that dihydroceramide accumulation in *DEGS1/ifc*-compromised neurons leads to mislocalization of active Rac1 to endolysosomes and Rac1/NOX-dependent neurodegeneration. Dihydroceramide is a neurotoxic intermediate of sphingolipid biosynthesis, and its accumulation is associated with neurological disorders. By a combination of experiments in a genetic model and in cultured human cells, our study describes a cellular mechanism underlying *DEGS1/ifc*-associated neurodegeneration and provides molecular insights into sphingolipid biology and potential therapeutic strategies.

STAR★METHODS

Detailed methods are provided in the online version of this paper and include the following:

- KEY RESOURCES TABLE
- RESOURCE AVAILABILITY
  - Lead contact
  - Materials availability
  - Data and code availability
- EXPERIMENTAL MODELS AND SUBJECT DETAILS
  - *Drosophila* strains and genetics
  - Cell line
- METHOD DETAILS
  - Immunohistochemistry and microscopy
  - Electroretinogram (ERG)
  - roGFP reporter: Cloning and assays
  - Western blotting
  - DEGS1^{H132R} CRISPR knock-in SH-SY5Y cells
  - DHE staining, and measurement of neurite length analysis
  - Sphingolipidomics
  - Subcellular fractionation
  - Isolation of SH-SY5Y cell membrane rafts
  - Amplex Red-HRP assay
  - Rac1-liposome binding assay
- QUANTIFICATION AND STATISTICAL ANALYSIS

SUPPLEMENTAL INFORMATION

Supplemental information can be found online at https://doi.org/10.1016/j.celrep.2021.108972.

ACKNOWLEDGMENTS

We thank Drs. Robin Hiesinger, Jennifer Jin, and Ya-Wen Liu and all members of the Chan and Huang labs for critical comments on this manuscript. We also thank Drs. Hwei-Jan Hsu, Ya-Wen Liu, Shu-Chun Teng, and Chia-Wei Yang; the Bloomington Drosophila Stock Center; the Drosophila Genetic Resource Center at the Kyoto Institute of Technology; the Vienna Drosophila Resource Center; the Developmental Studies Hybridoma Bank; the Drosophila Transgenic RNAi Project at Harvard Medical School; and the Zurich ORFeome Project for fly strains, reagents, and equipment. We further thank Wellgenetics for fly injection services and the staff of the Imaging, the Gene Knockout/in Cell Line Modeling, and the Biomedical Resource Cores at the First Core Labs at the National Taiwan University College of Medicine for technical assistance. We also thank Dr. Marcus Calkins for professional English editing service. This work was supported by grants from the Ministry of Science and Technology of Taiwan (MOST) (107WFA0111977) to S.-Y.H. and MOST (108-2321-B-002-060-MY2 and 108-2311-B-002-011-MY3), National Taiwan University (NTU) (109L104308 and 109L893603), and NTU Hospital (109C101-10-1) to C.-C.C.

AUTHOR CONTRIBUTIONS

Conceptualization, F.-Y.T., T.-Y.S., C.-C.L., S.-Y.H., and C.-C.C.; investigation, F.-Y.T., T.-Y.S., W.-S.L., Y.-H.Y., Y.-L.Y., and H.-C.K.; writing – original draft, F.-Y.T. and T.-Y.S.; writing – review & editing, C.-H.K., S.-Y.H., and C.-C.C.; funding acquisition, S.-Y.H. and C.-C.C.; supervision, C.-C.C.

DECLARATION OF INTERESTS

The authors declare no competing interests.

INCLUSION AND DIVERSITY

We worked to ensure sex balance in the selection of non-human subjects. The author list of this paper includes contributors from the location where the research was conducted who participated in the data collection, design, analysis, and/or interpretation of the work.

Received: June 3, 2020
Revised: January 18, 2021
Accepted: March 19, 2021
Published: April 13, 2021

REFERENCES

Abreu-Blanco, M.T., Verboon, J.M., and andParkhurst, S.M. (2014). Coordination of Rho family GTPase activities to orchestrate cytoskeleton responses during cell wound repair. Curr. Biol. *24*, 144–155.

Alanko, S.M.K., Halling, K.K., Maunula, S., Slotte, J.P., and Ramstedt, B. (2005). Displacement of sterols from sterol/sphingomyelin domains in fluid bilayer membranes by competing molecules. Biochim. Biophys. Acta *1715*, 111–121.

Albrecht, S.C., Barata, A.G., Grosshans, J., Teleman, A.A., and Dick, T.P. (2011). *In vivo* mapping of hydrogen peroxide and oxidized glutathione reveals chemical and regional specificity of redox homeostasis. Cell Metab. *14*, 819–829.

Angelova, P.R., and Abramov, A.Y. (2018). Role of mitochondrial ROS in the brain: from physiology to neurodegeneration. FEBS Lett. *592*, 692–702.

Barth, B.M., Gustafson, S.J., and Kuhn, T.B. (2012). Neutral sphingomyelinase activation precedes NADPH oxidase-dependent damage in neurons exposed to the proinflammatory cytokine tumor necrosis factor-α. J. Neurosci. Res. *90*, 229–242.

Bejaoui, K., Wu, C., Scheffler, M.D., Haan, G., Ashby, P., Wu, L., de Jong, P., and Brown, R.H., Jr. (2001). SPTLC1 is mutated in hereditary sensory neuropathy, type 1. Nat. Genet. *27*, 261–262.

Boesze-Battaglia, K. (2006). Isolation of Membrane Rafts and Signaling Complexes. Methods in Molecular Biology *332*, 169–179. https://doi.org/10.1385/1-59745-048-0:167.

Boslem, E., Weir, J.M., MacIntosh, G., Sue, N., Cantley, J., Meikle, P.J., and Biden, T.J. (2013). Alteration of endoplasmic reticulum lipid rafts contributes to lipotoxicity in pancreatic β-cells. J. Biol. Chem. *288*, 26569–26582.

Chung, H.L., Wangler, M.F., Marcogliese, P.C., Jo, J., Ravenscroft, T.A., Zuo, Z., Duraine, L., Sadeghzadeh, S., Li-Kroeger, D., Schmidt, R.E., et al. (2020). Loss- or Gain-of-Function Mutations in ACOX1 Cause Axonal Loss via Different Mechanisms. Neuron *106*, 589–606.

Cui, M., Ying, R., Jiang, X., Li, G., Zhang, X., Zheng, J., Tam, K.Y., Liang, B., Shi, A., Göbel, V., and Zhang, H. (2019). A Model of Hereditary Sensory and Autonomic Neuropathy Type 1 Reveals a Role of Glycosphingolipids in Neuronal Polarity. J. Neurosci. *39*, 5816–5834.

Czubowicz, K., and Strosznajder, R. (2014). Ceramide in the molecular mechanisms of neuronal cell death. The role of sphingosine-1-phosphate. Mol. Neurobiol. *50*, 26–37.

Dawkins, J.L., Hulme, D.J., Brahmbhatt, S.B., Auer-Grumbach, M., and Nicholson, G.A. (2001). Mutations in SPTLC1, encoding serine palmitoyltransferase, long chain base subunit-1, cause hereditary sensory neuropathy type I. Nat. Genet. *27*, 309–312.

Dawson, T.M., and Dawson, V.L. (2018). Nitric Oxide Signaling in Neurodegeneration and Cell Death. Adv. Pharmacol. *82*, 57–83.

del Pozo, M.A., Alderson, N.B., Kiosses, W.B., Chiang, H.H., Anderson, R.G., and Schwartz, M.A. (2004). Integrins Regulate Rac Targeting by Internalization of Membrane Domains. Science *303*, 839–842.

Di Pardo, A., Basit, A., Armirotti, A., Amico, E., Castaldo, S., Pepe, G., Marracino, F., Buttari, F., Digilio, A.F., and Maglione, V. (2017). *De novo* synthesis of sphingolipids is defective in experimental models of Huntington's disease. Front. Neurosci. *11*, 698.

Dolgin, V., Straussberg, R., Xu, R., Mileva, I., Yogev, Y., Khoury, R., Konen, O., Barhum, Y., Zvulunov, A., Mao, C., and Birk, O.S. (2019). DEGS1 variant causes neurological disorder. Eur. J. Hum. Genet. *27*, 1668–1676.

Fekry, B., Jeffries, K.A., Esmaeilniakooshkghazi, A., Szulc, Z.M., Knagge, K.J., Kirchner, D.R., Horita, D.A., Krupenko, S.A., and Krupenko, N.I. (2018). C_{16}-ceramide is a natural regulatory ligand of p53 in cellular stress response. Nat. Commun. *9*, 4149.

Fonteh, A.N., Ormseth, C., Chiang, J., Cipolla, M., Arakaki, X., and Harrington, M.G. (2015). Sphingolipid metabolism correlates with cerebrospinal fluid Beta amyloid levels in Alzheimer's disease. PLoS ONE *10*, e0125597.

Godeiro Junior, C.O., Vale, T.C., Afonso, C.O.M., Kok, F., Pedroso, J.L., and Barsottini, O.G. (2018). Progressive Myoclonic Epilepsy Type 8 Due to CERS1 Deficiency: A Novel Mutation with Prominent Ataxia. Mov. Disord. Clin. Pract. (Hoboken) *5*, 330–332.

Grassmé, H., Jekle, A., Riehle, A., Schwarz, H., Berger, J., Sandhoff, K., Kolesnick, R., and Gulbins, E. (2001). CD95 signaling via ceramide-rich membrane rafts. J. Biol. Chem. *276*, 20589–20596.

Hanson, G.T., Aggeler, R., Oglesbee, D., Cannon, M., Capaldi, R.A., Tsien, R.Y., and Remington, S.J. (2004). Investigating mitochondrial redox potential with redox-sensitive green fluorescent protein indicators. J. Biol. Chem. *279*, 13044–13053.

Honorat, J.A., Kinoshita, M., Okuno, T., Takata, K., Koda, T., Tada, S., Shirakura, T., Fujimura, H., Mochizuki, H., Sakoda, S., and Nakatsuji, Y. (2013). Xanthine oxidase mediates axonal and myelin loss in a murine model of multiple sclerosis. PLoS ONE *8*, e71329.

Hunot, S., Brugg, B., Ricard, D., Michel, P.P., Muriel, M.P., Ruberg, M., Faucheux, B.A., Agid, Y., and Hirsch, E.C. (1997). Nuclear translocation of NF-kappaB is increased in dopaminergic neurons of patients with parkinson disease. Proc. Natl. Acad. Sci. USA *94*, 7531–7536.

Jung, W.H., Liu, C.C., Yu, Y.L., Chang, Y.C., Lien, W.Y., Chao, H.C., Huang, S.Y., Kuo, C.H., Ho, H.C., and Chan, C.C. (2017). Lipophagy prevents activity-dependent neurodegeneration due to dihydroceramide accumulation *in vivo*. EMBO Rep. *18*, 1150–1165.

Kajimoto, T., Shirai, Y., Sakai, N., Yamamoto, T., Matsuzaki, H., Kikkawa, U., and Saito, N. (2004). Ceramide-induced apoptosis by translocation, phosphorylation, and activation of protein kinase Cdelta in the Golgi complex. J. Biol. Chem. *279*, 12668–12676.

Karsai, G., Kraft, F., Haag, N., Korenke, G.C., Hänisch, B., Othman, A., Suriyanarayanan, S., Steiner, R., Knopp, C., Mull, M., et al. (2019). DEGS1-associated aberrant sphingolipid metabolism impairs nervous system function in humans. J. Clin. Invest. *129*, 1229–1239.

Kinoshita, M., Tanaka, K., and Matsumori, N. (2020). The influence of ceramide and its dihydro analog on the physico-chemical properties of sphingomyelin bilayers. Chem. Phys. Lipids *226*, 104835.

Kulakowski, G., Bousquet, H., Manneville, J.B., Bassereau, P., Goud, B., and Oesterlin, L.K. (2018). Lipid packing defects and membrane charge control RAB GTPase recruitment. Traffic *19*, 536–545.

Laleu, B., Gaggini, F., Orchard, M., Fioraso-Cartier, L., Cagnon, L., Houngninou-Molango, S., Gradia, A., Duboux, G., Merlot, C., Heitz, F., et al. (2010). First in class, potent, and orally bioavailable NADPH oxidase isoform 4 (Nox4) inhibitors for the treatment of idiopathic pulmonary fibrosis. J. Med. Chem. *53*, 7715–7730.

Laviad, E.L., Albee, L., Pankova-Kholmyansky, I., Epstein, S., Park, H., Merrill, A.H., Jr., and Futerman, A.H. (2008). Characterization of ceramide synthase 2: tissue distribution, substrate specificity, and inhibition by sphingosine 1-phosphate. J. Biol. Chem. *283*, 5677–5684.

Magalhaes, M.A.O., and Glogauer, M. (2010). Pivotal Advance: Phospholipids determine net membrane surface charge resulting in differential localization of active Rac1 and Rac2. J. Leukoc. Biol. *87*, 545–555.

Mielke, M.M., Haughey, N.J., Bandaru, V.V.R., Weinberg, D.D., Darby, E., Zaidi, N., Pavlik, V., Doody, R.S., and Lyketsos, C.G. (2011). Plasma sphingomyelins are associated with cognitive progression in Alzheimer's disease. J. Alzheimers Dis. *27*, 259–269.

Morgan, B., Sobotta, M.C., and Dick, T.P. (2011). Measuring E(GSH) and H2O2 with roGFP2-based redox probes. Free Radic. Biol. Med. *51*, 1943–1951.

Mosbech, M.B., Olsen, A.S.B., Neess, D., Ben-David, O., Klitten, L.L., Larsen, J., Sabers, A., Vissing, J., Nielsen, J.E., Hasholt, L., et al. (2014). Reduced ceramide synthase 2 activity causes progressive myoclonic epilepsy. Ann. Clin. Transl. Neurol. *1*, 88–98.

Oswald, M.C.W., West, R.J.H., Lloyd-Evans, E., and Sweeney, S.T. (2015). Identification of dietary alanine toxicity and trafficking dysfunction in a Drosophila model of hereditary sensory and autonomic neuropathy type 1. Hum. Mol. Genet. *24*, 6899–6909.

Pant, D.C., Dorboz, I., Schluter, A., Fourcade, S., Launay, N., Joya, J., Aguilera-Albesa, S., Yoldi, M.E., Casasnovas, C., Willis, M.J., et al. (2019). Loss of the sphingolipid desaturase DEGS1 causes hypomyelinating leukodystrophy. J. Clin. Invest. *129*, 1240–1256.

Payapilly, A., and Malliri, A. (2018). Compartmentalisation of RAC1 signalling. Curr. Opin. Cell Biol. *54*, 50–56.

Prado Spalm, F.H., Vera, M.S., Dibo, M.J., Simón, M.V., Politi, L.E., and Rotstein, N.P. (2019). Ceramide Induces the Death of Retina Photoreceptors Through Activation of Parthanatos. Mol. Neurobiol. *56*, 4760–4777.

Qin, J., Berdyshev, E., Goya, J., Natarajan, V., and Dawson, G. (2010). Neurons and oligodendrocytes recycle sphingosine 1-phosphate to ceramide: significance for apoptosis and multiple sclerosis. J. Biol. Chem. *285*, 14134–14143.

Rao, Y., Perna, M.G., Hofmann, B., Beier, V., and Wollert, T. (2016). The Atg1-kinase complex tethers Atg9-vesicles to initiate autophagy. Nat. Commun. *7*, 10338.

Resh, M.D. (2004). Membrane Targeting of Lipid Modified Signal Transduction Proteins. Subcell. Biochem. *37*, 217–232.

Rodriguez-Cuenca, S., Barbarroja, N., and Vidal-Puig, A. (2015). Dihydroceramide desaturase 1, the gatekeeper of ceramide induced lipotoxicity. Biochim. Biophys. Acta *1851*, 40–50.

Rotthier, A., Auer-Grumbach, M., Janssens, K., Baets, J., Penno, A., Almeida-Souza, L., Van Hoof, K., Jacobs, A., De Vriendt, E., Schlotter-Weigel, B., et al. (2010). Mutations in the SPTLC2 subunit of serine palmitoyltransferase cause

hereditary sensory and autonomic neuropathy type I. Am. J. Hum. Genet. *87*, 513–522.

Schindelin, J., Arganda-Carreras, I., Frise, E., Kaynig, V., Longair, M., Pietzsch, T., Preibisch, S., Rueden, C., Saalfeld, S., Schmid, B., et al. (2012). Fiji: an open-source platform for biological-image analysis. Nat. Methods *9*, 676–682.

Siddique, M.M., Li, Y., Chaurasia, B., Kaddai, V.A., and Summers, S.A. (2015). Dihydroceramides: From bit players to lead actors. J. Biol. Chem. *290*, 15371–15379.

Snow, B.J., Rolfe, F.L., Lockhart, M.M., Frampton, C.M., O'Sullivan, J.D., Fung, V., Smith, R.A.J., Murphy, M.P., and Taylor, K.M.; Protect Study Group (2010). A double-blind, placebo-controlled study to assess the mitochondria-targeted antioxidant MitoQ as a disease-modifying therapy in Parkinson's disease. Mov. Disord. *25*, 1670–1674.

Sorce, S., Stocker, R., Seredenina, T., Holmdahl, R., Aguzzi, A., Chio, A., Depaulis, A., Heitz, F., Olofsson, P., Olsson, T., et al. (2017). NADPH oxidases as drug targets and biomarkers in neurodegenerative diseases: What is the evidence? Free Radic. Biol. Med. *112*, 387–396.

Vanni, N., Fruscione, F., Ferlazzo, E., Striano, P., Robbiano, A., Traverso, M., Sander, T., Falace, A., Gazzerro, E., Bramanti, P., et al. (2014). Impairment of ceramide synthesis causes a novel progressive myoclonus epilepsy. Ann. Neurol. *76*, 206–212.

Volpert, G., Ben-Dor, S., Tarcic, O., Duan, J., Saada, A., Merrill, A.H., Jr., Pewzner-Jung, Y., and Futerman, A.H. (2017). Oxidative stress elicited by modifying the ceramide acyl chain length reduces the rate of clathrin-mediated endocytosis. J. Cell Sci. *130*, 1486–1493.

Wu, J., Ma, S., Sandhoff, R., Ming, Y., Hotz-Wagenblatt, A., Timmerman, V., Bonello-Palot, N., Schlotter-Weigel, B., Auer-Grumbach, M., Seeman, P., et al. (2019). Loss of Neurological Disease HSAN-I-Associated Gene SPTLC2 Impairs $CD8^+$ T Cell Responses to Infection by Inhibiting T Cell Metabolic Fitness. Immunity *50*, 1218–1231.e5.

Zhu, Z., Chen, J., Wang, G., Elsherbini, A., Zhong, L., Jiang, X., Qin, H., Tripathi, P., Zhi, W., Spassieva, S.D., et al. (2019). Ceramide regulates interaction of Hsd17b4 with Pex5 and function of peroxisomes. Biochim. Biophys. Acta Mol. Cell Biol. Lipids *1864*, 1514–1524.

STAR★METHODS

KEY RESOURCES TABLE

Reagents or Resources	Source	Identifier
Antibodies		
Anti-ifc	Jung et al., 2017	N/A
Anti-Rab7	Jung et al., 2017	N/A
Na^+/K^+-ATPase	Developmental Studies Hybridoma Bank	DSHB Cat# a5; RRID:AB_2166869
Anti-EEA-1	Developmental Studies Hybridoma Bank	RRID:AB_2618586
Anti-GABARAP	Abcam	Abcam Cat# ab109364; RRID:AB_10861928
Anti-Rab7	Abcam	Abcam Cat# ab137029; RRID:AB_2629474
Anti-Calnexin	Abcam	Abcam Cat# ab75801; RRID:AB_1310022
Anti-ATP5A	Abcam	Abcam Cat# ab14748; RRID:AB_301447
Anti-Active Rac1-GTP	NewEast Biosciences	NewEast Biosciences Cat# 26903; RRID:AB_1961793
Anti-Rac1	BD Bioscience	BD Biosciences Cat# 610650; RRID:AB_397977
Anti-Actin	Merck Millipore	Millipore Cat# MAB1501; RRID:AB_2223041
Anti-Flotillin-2	Cell Signaling Technology	Cell Signaling Technology Cat# 3436; RRID:AB_2106572
Anti-TOM20	Cell Signaling Technology	Cell Signaling Technology Cat# 42406; RRID:AB_2687663
Alexa Fluor®-647 anti-Rabbit IgG	Jackson ImmunoResearch Laboratories	Jackson ImmunoResearch Labs Cat# 111-605-003; RRID:AB_2338072
Alexa Fluor®-488 anti-Mouse IgG	Jackson ImmunoResearch Laboratories	Jackson ImmunoResearch Labs Cat# 715-545-150; RRID:AB_2340846
Alexa Fluor®-488 anti-Rabbit IgG	Jackson ImmunoResearch Laboratories	Jackson ImmunoResearch Labs Cat# 711-545-152; RRID:AB_2313584
Cy3 anti-Rabbit IgG	Jackson ImmunoResearch Laboratories	Jackson ImmunoResearch Labs Cat# 111-165-003; RRID:AB_2338000
HRP anti-Rabbit IgG	Jackson ImmunoResearch Laboratories	Jackson ImmunoResearch Labs Cat# 111-035-003; RRID:AB_2313567
HRP anti-Mouse IgG	Jackson ImmunoResearch Laboratories	Jackson ImmunoResearch Labs Cat# 115-035-003; RRID:AB_10015289
Alexa Fluor®-488-phalloidin	Invitrogen	Thermo Fisher Scientific Cat# A12379
DyLight-405 anti-mouse IgG	Invitrogen	Thermo Fisher Scientific Cat# 35501BID; RRID:AB_2533209
Chemicals, peptides, and recombinant proteins		
1-palmitoyl-2-oleoyl-glycero-3-phosphocholine (16:0-18:1 PC)	AvantiLipids	850457
1-palmitoyl-2-oleoyl-sn-glycero-3-phospho-L-serine (sodium salt) (16:0-18:1 PS)	AvantiLipids	840034
1-palmitoyl-2-oleoyl-sn-glycero-3-phosphoethanolamine (16:0-18:1 PE)	AvantiLipids	850757
1,2-dioleoyl-sn-glycero-3-phospho-(1'-myo-inositol-3′-phosphate) (ammonium salt) (18:1 PI(3)P)	AvantiLipids	850150
Sphingomyelin (Brain, Porcine)	AvantiLipids	860062

(*Continued on next page*)

Continued

Reagents or Resources	Source	Identifier
N-stearoyl-D-erythro-sphinganine (C18-Dihydroceramide (d18:0/18:0))	AvantiLipids	860627
N-stearoyl-D-erythro-sphingosine (C18-Ceramide (d18:1/18:0))	AvantiLipids	860518
Cholesterol	Sigma	C8667
Apocynin	Sigma	W508454
Allopurinol	Sigma	A8003
L-NAME	Sigma	N5751
GKT136901	Sigma	5.34032
Experimental models: Cell lines		
Human: SH-SY5Y cells	ATCC	CRL-2266
Experimental models: *Drosophila* strains		
w[1118]; ifc-KO, P{ry[+t7.2] = neoFRT}40A	Jung et al., 2017	N/A
y[d2] w[1118] P{ry[+t7.2] = ey-FLP.N}2 P {5xglBS-lacZ.38-1}TPN1; P{ry[+t7.2] = neoFRT}40A	Bloomington Drosophila Stock Center	RRID:BDSC_5615
w[1118]	Bloomington Drosophila Stock Center	RRID:BDSC_3605
y[d2] w[1118] P{ry[+t7.2] = ey-FLP.N}2 P {5xglBS-lacZ.38-1}TPN1; l(2)cl-L3[1] P{w [+m] ry[+t7.2] = white-un1}30C P{ry [+t7.2] = neoFRT}40A/CyO, y[+]*	Bloomington Drosophila Stock Center	RRID:BDSC_5622
y[1] w[1118]; P{w[+mC] = Ubi-mRFP.nls}2L P{ry[+t7.2] = neoFRT}40A/CyO	Bloomington Drosophila Stock Center	RRID:BDSC_34500
w[1118] P{ry[+t7.2] = ey-FLP.N}2; P{w [+mC] = GMR-myr-mRFP}2L P{ry[+t7.2] = neoFRT}40A/CyO	Bloomington Drosophila Stock Center	RRID:BDSC_7122
w[1118]; P{w[+mC] = UAS-Sod1}12.1 (chromosome hopping from 2 to 3)	Bloomington Drosophila Stock Center	RRID:BDSC_33605
w[1]; P{w[+mC] = UAS-Sod2.M}UM83 (chromosome hopping from 2 to 3)	Bloomington Drosophila Stock Center	RRID:BDSC_24494
w[1]; P{w[+mC] = UAS-Cat.A}2 (chromosome hopping from 2 to 3)	Bloomington Drosophila Stock Center	RRID:BDSC_24621
w[*]; P{w[+mC] = GFP-Rac1}30	Bloomington Drosophila Stock Center	RRID:BDSC_52285
w[*]; P{w[+mC] = sqh-Pak1.RBD-GFP}31/ TM3, Sb[1]	Bloomington Drosophila Stock Center	RRID:BDSC_56550
y[1] v[1]; P{y[+t7.7] v[+t1.8] = TRiP.JF02813} attP2 e[*]	Bloomington Drosophila Stock Center	RRID:BDSC_28985
y[1] sc[*] v[1] sev[21]; P{y[+t7.7] v[+t1.8] = TRiP.HMS00429}attP2	Bloomington Drosophila Stock Center	RRID:BDSC_32433
y[1] sc[*] v[1] sev[21]; P{y[+t7.7] v[+t1.8] = TRiP.HMS00691}attP2	Bloomington Drosophila Stock Center	RRID:BDSC_32902
w[1118]; P{w[+mC] = UAS-cyto-Grx1-roGFP2}13 (chromosome hopping from 2 to 3)	Bloomington Drosophila Stock Center	RRID:BDSC_67662
w[1118]; P{w[+mC] = UAS-mito-roGFP2-Grx1}9 (chromosome hopping from 2 to 3)	Bloomington Drosophila Stock Center	RRID:BDSC_67667
Oligonucleotides		
DEGS1^{H132R} gRNA forward oligo (5′ AAACACCGGTATCACATGGATCATCAT)	This paper	N/A
DEGS1^{H132R} gRNA reverse oligo (5′ CTCTAAAACATGATGATCCATGTGATAC)	This paper	N/A

(*Continued on next page*)

Continued

Reagents or Resources	Source	Identifier
DEGS1^{H132R} sequencing forward primer (5′ TTTGGGGCCTATGCGTTTGG)	This paper	N/A
DEGS1^{H132R} reverse primer (5′ GTGCAAACCCAGGCCAAGTA)	This paper	N/A
Cyto-roGFP-CAAX primer 1 (5′ CCCGGGATCCACCGGTCGCC)	This paper	N/A
Cyto-roGFP-CAAX primer 2 (5′ TGCA GCCTGAATTCGAAGCTTGAGCTCGA GATCTGAGTCCGGACTTGTACAGCT CGTCCA)	This paper	N/A
Cyto-roGFP-CAAX primer 3 (5′ CCCG CTGTGGCGGCCGCTCAGGAGAGCA CACACTTG CAGCTCATGCAGCCTGAATTCGAA)	This paper	N/A
Recombinant DNA		
Plasmid: cyto-roGFP	Addgene	RRID:Addgene_49435
Plasmid: cyto-roGFP-CAAX	This paper	N/A

RESOURCE AVAILABILITY

Lead contact

Further information and requests for resources and reagents should be directed to and will be fulfilled by the Lead Contact, Chih-Chiang Chan (chancc1@ntu.edu.tw).

Materials availability

Fly stocks and plasmids generated in this study can be requested and may require a material transfer agreement.

Data and code availability

All relevant data are available from the lead contact upon reasonable request.

EXPERIMENTAL MODELS AND SUBJECT DETAILS

Drosophila strains and genetics

Drosophila stocks and crosses were maintained at 25°C on standard medium following standard fly husbandry. Information on individual fly strains can be found on FlyBase (flybase.org) unless otherwise noted (Key Resources Table).

For light stimulation, flies were exposed to constant 1000 Lux light from a LED light source. Eye-specific mosaic clones were generated using ey-FLP on the X chromosome while whole-eye clones of ifc-KO photoreceptors were generated as previously described (Jung et al., 2017).

Following are the genotypes used in our analyses:

Controls — y[d2] w[1118] P{ry[+t7.2] = ey-FLP.N}2 P{5xglBS-lacZ.38-1}TPN1/+; l(2)cl-L3[1] P{w[+t*] ry[+t*] = white-un1}30C P{ry[+t7.2] = neoFRT}40A/ P{ry[+t7.2] = neoFRT}40A; P{y[+*] = GMR-GAL4,UAS-w.RNAi}3/+ (Figures 1A, 1E, 1K, 4A, 5P, 6A, 6C, 6E, 6G, and 6I; Figures S1A, S1E, S4A, S4B, S4E, and S4J); y[d2] w[1118] P{ry[+t7.2] = ey-FLP.N}2 P{5xglBS-lacZ.38-1}TPN1/+; l(2)cl-L3[1] P{w[+t*] ry[+t*] = white-un1}30C P{ry[+t7.2] = neoFRT}40A/ P{ry[+t7.2] = neoFRT}40A; P{y[+*] = GMR-GAL4,UAS-w.RNAi}3/P{UAS-cyto-Grx1-roGFP2}13 (Figure 1P); y[d2] w[1118] P{ry[+t7.2] = ey-FLP.N}2 P{5xglBS-lacZ.38-1}TPN1/+; l(2)cl-L3[1] P{w[+t*] ry[+t*] = white-un1}30C P{ry[+t7.2] = neoFRT}40A/ P{ry[+t7.2] = neoFRT}40A; P{y[+*] = GMR-GAL4,UAS-w.RNAi}3/P{UAS-mito-roGFP2-Grx1}9 (Figure 1R; Figure S1K).

ifc-KO whole eye clones — y[d2] w[1118] P{ry[+t7.2] = ey-FLP.N}2 P{5xglBS-lacZ.38-1}TPN1/+; l(2)cl-L3[1] P{w[+t*] ry[+t*] = white-un1}30C P{ry[+t7.2] = neoFRT}40A/ ifc-KO, P{ry[+t7.2] = neoFRT}40A; P{y[+*] = GMR-GAL4,UAS-w.RNAi}3/+ (Figures 1B, 1G, 1L, 4A, 4C, 4D, 4F–4I, 4K–4O, 5A–5D, 5J, 5Q, 5R, 6B, 6D, 6F, 6H, and 6J; Figure S1B); y[d2] w[1118] P{ry[+t7.2] = ey-FLP.N}2 P{5xglBS-lacZ.38-1}TPN1/+; l(2)cl-L3[1] P{w[+t*] ry[+t*] = white-un1}30C P{ry[+t7.2] = neoFRT}40A/ ifc-KO, P{ry[+t7.2] = neoFRT}40A; P{y[+*] = GMR-GAL4,UAS-w.RNAi}3/P{UAS-cyto-Grx1-roGFP2}13 (Figure 1Q); y[d2] w[1118] P{ry[+t7.2] = ey-FLP.N}2 P{5xglBS-lacZ.38-1}TPN1/+; l(2)cl-L3[1] P{w[+t*] ry[+t*] = white-un1}30C P{ry[+t7.2] = neoFRT}40A/ ifc-KO, P{ry[+t7.2] = neoFRT}40A; P{y[+*] = GMR-GAL4,UAS-w.RNAi}3/P{UAS-mito-roGFP2-Grx1}9 (Figure 1S).

SOD1 rescue experiment — y[d2] w[1118] P{ry[+t7.2] = ey-FLP.N}2 P{5xglBS-lacZ.38-1}TPN1/+; l(2)cl-L3[1] P{w[+t*] ry[+t*] = white-un1}30C P{ry[+t7.2] = neoFRT}40A/ ifc-KO, P{ry[+t7.2] = neoFRT}40A; P{y[+*] = GMR-GAL4,UAS-w.RNAi}3/P{w[+mC] = UAS-Sod1}12.1 (Figures 1C, 1H, and 1M).
SOD2 rescue experiment — y[d2] w[1118] P{ry[+t7.2] = ey-FLP.N}2 P{5xglBS-lacZ.38-1}TPN1/+; l(2)cl-L3[1] P{w[+t*] ry[+t*] = white-un1}30C P{ry[+t7.2] = neoFRT}40A/ ifc-KO, P{ry[+t7.2] = neoFRT}40A; P{y[+*] = GMR-GAL4,UAS-w.RNAi}3/P{w[+mC] = UAS-Sod2.M}UM83 (Figures 1D, 1I, and 1N).
Catalase rescue experiment — y[d2] w[1118] P{ry[+t7.2] = ey-FLP.N}2 P{5xglBS-lacZ.38-1}TPN1/+; l(2)cl-L3[1] P{w[+t*] ry[+t*] = white-un1}30C P{ry[+t7.2] = neoFRT}40A/ ifc-KO, P{ry[+t7.2] = neoFRT}40A; P{y[+*] = GMR-GAL4,UAS-w.RNAi}3/P{UAS-Cat.A}2 (Figures S1C and S1G).
ifc-KO mosaic eye clones — w[1118] P{ry[+t7.2] = ey-FLP.N}2; P{w[+mC] = GMR-myr-mRFP}2L P{ry[+t7.2] = neoFRT}40A/ifc-KO, P{ry[+t7.2] = neoFRT}40A; P{GFP-Rac1}30/+ (Figure 4C); w[1118] P{ry[+t7.2] = ey-FLP.N}2; P{w[+mC] = GMR-myr-mRFP}2L P{ry[+t7.2] = neoFRT}40A/ifc-KO, P{ry[+t7.2] = neoFRT}40A; P{GFP-Rac1}30/+ (Figure 4C); w[1118] P{ry[+t7.2] = ey-FLP.N}2; P{w[+mC] = GMR-myr-mRFP}2L P{ry[+t7.2] = neoFRT}40A/ifc-KO, P{ry[+t7.2] = neoFRT}40A; P{sqh-Pak1.RBD-GFP}31/+ (Figure 4D); w[1118] P{ry[+t7.2] = ey-FLP.N}2; P{w[+mC] = GMR-myr-mRFP}2L P{ry[+t7.2] = neoFRT}40A/ifc-KO, P{ry[+t7.2] = neoFRT}40A; P{y[+*] = GMR-GAL4,UAS-w.RNAi}3/P{UAS-cyto-Grx1-roGFP2}13 (Figure S1I); w[1118] P{ry[+t7.2] = ey-FLP.N}2; P{w[+mC] = GMR-myr-mRFP}2L P{ry[+t7.2] = neoFRT}40A/ifc-KO, P{ry[+t7.2] = neoFRT}40A; P{y[+*] = GMR-GAL4,UAS-w.RNAi}3/ P{UAS-mito-roGFP2-Grx1}9 (Figure S1J).
Rac1 heterozygote rescue experiment — y[d2] w[1118] P{ry[+t7.2] = ey-FLP.N}2 P{5xglBS-lacZ.38-1}TPN1/+; l(2)cl-L3[1] P{w[+t*] ry[+t*] = white-un1}30C P{ry[+t7.2] = neoFRT}40A/ ifc-KO, P{ry[+t7.2] = neoFRT}40A; P{y[+*] = GMR-GAL4,UAS-w.RNAi}3/Rac1 [J11] P{w[+mW.hs] = FRT(w[hs])}2A (Figures 5A and 5N)
Rac1 RNAi rescue experiment — y[d2] w[1118] P{ry[+t7.2] = ey-FLP.N}2 P{5xglBS-lacZ.38-1}TPN1/+; l(2)cl-L3[1] P{w[+t*] ry[+t*] = white-un1}30C P{ry[+t7.2] = neoFRT}40A/ ifc-KO, P{ry[+t7.2] = neoFRT}40A; P{y[+*] = GMR-GAL4,UAS-w.RNAi}3/P{TRiP.JF02813}attP2 (Figures 5B and 5M)
NOX RNAi rescue experiment — y[d2] w[1118] P{ry[+t7.2] = ey-FLP.N}2 P{5xglBS-lacZ.38-1}TPN1/+; l(2)cl-L3[1] P{w[+t*] ry[+t*] = white-un1}30C P{ry[+t7.2] = neoFRT}40A/ ifc-KO, P{ry[+t7.2] = neoFRT}40A; P{y[+*] = GMR-GAL4,UAS-w.RNAi}3/P{TRiP.HMS00691}attP2 (Figures 5C and 5K); y[d2] w[1118] P{ry[+t7.2] = ey-FLP.N}2 P{5xglBS-lacZ.38-1}TPN1/+; l(2)cl-L3[1] P{w[+t*] ry[+t*] = white-un1}30C P{ry[+t7.2] = neoFRT}40A/ ifc-KO, P{ry[+t7.2] = neoFRT}40A; P{y[+*] = GMR-GAL4,UAS-w.RNAi}3/P{TRiP.HMS00429}attP2 (Figures 5D and 5L)

Cell line

The wild-type, *DEGS1*$^{KO/H132R}$ and *DEGS1*$^{H132R/H132R}$ knock-in SH-SY5Y human neuroblastoma cells were cultured in DMEM/F12 medium (GIBCO, 12500062) supplemented with 10% fetal bovine serum (GIBCO, A3160502) and maintained at 37°C in a 5% CO_2 humidified incubator. The cells were passaged when reaching confluency, usually every 7 days.

METHOD DETAILS

Immunohistochemistry and microscopy

For immunofluorescence staining, adult retina tissues were dissected in Phosphate-buffered saline (PBS), fixed in 4% paraformaldehyde for 20 minutes, and washed three times for 15 minutes each in PBS with 0.4% Triton X-100 (0.4% PBST). Fixed retina tissues were incubated with primary antibodies diluted in 0.4% PBST overnight at 4°C. After primary antibody incubation, samples were washed in 0.4% PBST three times for 10 minutes, followed by secondary antibody incubation overnight at 4°C. On the next day, the samples were washed again three times in 0.4% PBST for 10 minutes before mounted in VECTASHIELD (Vector Laboratories). ROS detection was performed with 10 μM of CM-H_2DCFDA (chloromethyl-2′,7′-dichlorodihydrofluorescein diacetate, Thermo Fisher, C6827) following the manufacturer's protocol. Samples were analyzed on either a Leica TCS SP5 confocal microscope with LAS AF software or a Zeiss LSM 880 confocal microscope with Zen software. Imaging data were processed and quantified using the Fiji package of ImageJ (National Institutes of Health) (Schindelin et al., 2012).

Electroretinogram (ERG)

ERGs were performed as previously described (Jung et al., 2017). In brief, flies were immobilized on glass slides, and the ERGs were recorded upon one second light-on and light-off cycles with the recording and reference electrodes filled with 2 M NaCl. All experiments were carried out in triplicates with minimally 10 recordings per replicate for each genotype and experimental condition.

roGFP reporter: Cloning and assays

roGFP fly strains obtained from the Bloomington *Drosophila* stock center (Key resources table) were recombined into *ifc*-KO background, and mosaic clones were generated to compare the roGFP activity between the control and *ifc*-KO clones. After light exposure for 5 days, the flies were dissected following the aforementioned immunohistochemistry protocol. RoGFP is a reversible, redox-sensing form of GFP because of two surface cysteine insertions. The reduced form of roGFP has two excitation peaks at 405 nm and 488 nm, and one emission peak at 510 nm. Upon oxidation, the excitability at 488 nm greatly diminishes while the

405 nm peak increases. Thus, an increased ratio of 405nm-excited to 488nm-excited roGFPs signal indicates oxidation, as the excitation peak of oxidized roGFPs shifts from 488nm to 405nm(Hanson et al., 2004; Morgan et al., 2011).

For roGFP assays in SH-SY5Y cells, cyto-roGFP (Addgene, Plasmid #49435), and roGFP-CAAX plasmids were transfected by Lipofectamine 3000 (Thermo, L3000015) following the manufacturer's instructions. Transfected wild-type and *DEGS1*^{H132R} cells were seeded on cover slides for one day and mounted by VECTASHIED (Vector Laboratories, H-1000) before analyzed on an LSM880 microscope.

To generate cyto-roGFP-CAAX construct, the CAAX motif was cloned in-frame to the C terminus of the cyto-roGFP. In brief, cyto-roGFP-CAAX fragment were amplified by two PCR reactions with the primers listed below. The first reaction removed the stop codon of cyto-roGFP and added the first half of CAAX motif to the 3′ end (Primers 1 and 2). The second reaction added the second half of CAAX motif and a NotI cutting site to the previous PCR product (Primers 1 and 3). The resultant PCR product was digested by AgeI and NotI, and ligated with T4 ligase into the cyto-roGFP plasmid in replacement of the cyto-roGFP fragment cut by AgeI and NotI.

Primer 1: 5′- cccgggatccaccggtcgcc −3′
Primer 2: 5′- tgcagcctgaattcgaagcttgagctcgagatctgagtccggacttgtacagctcgtcca −3′
Primer 3: 5′-cccgctgtggcggccgctcaggagagcacacacttgcagctcatgcagcctgaattcgaa −3′

Western blotting

Protein extracts were separated by SDS-PAGE and transferred to polyvinylidene difluoride membranes (PVDF, Millipore, IPVH00010, pore size: 0.45 μm) as per manufacturer's instructions (Bio-Rad). PVDF membranes were incubated with 5% non-fat milk in TBST [10 mM Tris (pH 8.0), 150 mM NaCl, 0.1% Tween 20] for 1 hour at room temperature, washed three times with TBST for 10 minutes, and incubated with primary antibodies at 4°C overnight. Membranes were washed three times with TBST for 10 minutes before incubation with secondary antibodies in TBST for 1 hour at room temperature. Blots were then washed with TBST three times, developed with ECL reagents (Thermo, 34580; Millipore, WBKLS0500; or GE health, RPN2235), and captured by the BioSpectrum^{TM} 600 Imaging System (UVP Ltd).

DEGS1^{H132R} CRISPR knock-in SH-SY5Y cells

Human *DEGS1*^{H132R} knock-in point mutation was generated using the CRISPR/Cas9 system. The sgRNA design for CRISPR/Cas9 target sites was computationally identified at Zhang Lab's website (https://zlab.bio/guide-design-resources) and cloned by using the all-in-one plasmid construction Kit with dual selections of puromycin resistance and fluorescence (pZG22C02, ZGene Biotech Inc.). Trypsinized SH-SY5Y cells were washed with PBS once, and 1 × 10^5 cells mix with 2 μg plasmids plus 40 pmole single strand donor were used per electroporation (1100v/50ms/1pulses) using Neon^{TM} Transfection System 10 μl Kit (MPK1025, Thermo Fisher Scientific). The cells were plated into 24-well plates containing antibiotic-free complete medium and incubated at 37°C overnight in a 5% CO2 incubator before the selection with 0.5μg/ml puromycin for 2 days. A subset of the cells was harvested for the analysis of editing efficiencies, and the rest were diluted to 0.5 cells per well and plated into 96-well plates for single-cell cultures for at least one month. Half of the cells in each well were lysed for genomic PCR and the PCR products were treated with ExoSAP PCR clean-up reagent (75001, Thermo Fisher Scientific) and then send for sequencing. When the sequence results showed a pattern consistent with the target mutation, the PCR products were then cloned into a TA-cloning vector for blue-white selection. A total of 10 white colonies were selected and subjected to PCR amplification with M13 forward and reverse primers. The genomic PCR for detecting *DEGS1*^{H132R} knock-in SH-SY5Y was performed using the following primer set:

Forward primer: 5′-TTTGGGGCCTATGCGTTTGG-3′
Reverse primer: 5′-GTGCAAACCCAGGCCAAGTA-3′

The PCR products were cleaned and send for sequence confirmation Sequence data of the H132R knockin site were shown Figure 2A.

DHE staining, and measurement of neurite length analysis

For Dihydroethidium (DHE; Invitrogen, D11347) staining, cells were seeded on cover glasses (Glaswarenfabrik Karl Hecht GmbH, 41001118) in 12-well plates at a density of 1 × 10^5 cells per well. The wild-type or *DEGS1*^{H132R} knock-in SH-SY5Y cells were treated with DMSO, 50 μM apocynin, 100 μM Allopurinol, 50 μM L-NAME, or 10 μM GKT136901 for 24 h before incubating with 5 μM DHE in PBS (GIBCO, 10010-023) for 30 min at 37°C. Stained cells were washed with PBS and fixed with 4% paraformaldehyde (Electron Microscopy Sciences, 15710) in PBS for 10 min at room temperature. Fixed cells were washed with PBS, stained with 300 nM DAPI (Invitrogen, D1306) in PBS for 5 min at room temperature, and washed again with PBS. All samples were mounted in VECTASHIELD (Vector Laboratories, H-1000) and analyzed on a Zeiss Axio Imager M1 or LSM880 microscope.

For the measurement of neurite length, the wild-type and *DEGS1*^{H132R} knock-in SH-SY5Y cells were seeded on 6-well plates at a density of 1 × 10^5 cells/well and incubated overnight. Multiple images were taken under light microscopy and the captured images were labeled with a scale bar and quantified using Fiji (Schindelin et al., 2012).

Sphingolipidomics

Total cell and fractionated cell samples were extracted with 500 μL methanol:water = 4:1 (v/v) and 200 μL chloroform, and the extraction was performed by shaking at 1000rpm for 3 minutes by using a Geno/Grinder 2010 (SPEX SamplePrep., Metuchen, NJ, US). Then, 200 μL chloroform and 200 μL water were further added into the sample mixture followed by shaking on Geno/Grinder2010 with the parameters aforementioned. After that, the samples were put on ice for 15min and the extract was then centrifuged by using Eppendorf Centrifuge 5810R at 15000 x g for 5 minutes at 4°C. The lower layer of the supernatant was collected and dried under nitrogen gas, and then, stored at −20°C until analysis. Dried residue was reconstituted with 200 μL methanol containing 50 ng mL-1 internal standard ceramide (d18:1/17:0), and sonicated for 15 minutes followed by centrifuging at 15000 x g for 5 minutes at 4°C. Then, the supernatant was filtered with 0.2 μm Ministart RC 4 filter (Sartorius, Goettingen, Germany) and subjected to LC-MS/MS analysis.

Target ceramide metabolites were analyzed by Agilent 1290 UHPLC coupled with an Agilent 6460 triple quadrupole mass spectrometer (Agilent Technologies, Santa Clara, CA). The separation was performed using an Agilent ZORBAX Eclipse Plus C18 column (2.1 × 100 mm, 1.8 μm, Agilent Technologies, Santa Clara, CA), and the column was thermostated at 55°C during analysis. The mobile phase was composed of solvent A (10 mM ammonium acetate and 0.2% formic acid in methanol:water = 6:4, v/v) and solvent B (10 mM ammonium acetate and 0.2% formic acid in methanol:isopropanol = 6:4, v/v). A linear gradient elution was used: 0-2min, 35%–80% solvent B, 2-7min, 80%–100% solvent B, 7-14min, 100% solvent B, and column re-equilibration with 35% solvent B for 2 min. The flow rate was 0.35 mL min-1. The injection volume was 5 μL. The positive electrospray ionization mode was utilized with the following parameters: 325°C for drying gas temperature, 7 L min-1 for drying gas flow, 45 psi for nebulizer pressure, 325°C for sheath gas temperature, 11 L min-1 for sheath gas flow rate, and 3500 V for capillary voltage. Nozzle voltage was set at 500V. The mass spectrometer was configured in multiple reaction monitoring (MRM) mode, and the transitions for ceramide (d18:1/16:0) were m/z 538.5→264.3; dihydroceramide (d18:0/16:0) were m/z 540.5→266.3; ceramide (d18:1/17:0) were m/z 552.5→264.3; ceramide (d18:1/18:0) were m/z 566.5→264.3; dihydroceramide (d18:0/18:0) were m/z 568.5→266.3; ceramide (d18:1/20:0) were m/z 594.6→264.3; dihydroceramide (d18:0/20:0) were m/z 596.6→266.3; ceramide (d18:1/22:0) were m/z 622.6→264.3; dihydroceramide (d18:0/22:0) were m/z 624.6→266.3; ceramide (d18:1/22:1) were m/z 620.6→264.3; dihydroceramide (d18:0/22:1) were m/z 622.6→266.3; ceramide (d18:1/24:0) were m/z 650.6→264.3; dihydroceramide (d18:0/24:0) were m/z 652.6→266.3; ceramide (d18:1/24:1) were m/z 648.6→264.3; dihydroceramide (d18:0/24:1) were m/z 650.6→266.3. All the peaks were integrated with MassHunter Quantitative Analysis software (Agilent Technologies, Santa Clara, CA).

Subcellular fractionation

The subcellular fractionation was modified from a published protocol (Boslem et al., 2013). In brief, after washed twice on ice with PBS, ten 100 mm-plates of SH-SY5Y cells were scraped in ice-cold PBS and spun at 300 xg for 10 min to pellet cells. The pellet was resuspended in 1.3 mL of hypotonic buffer (10 mM HEPES, pH 7.4, 1 mM EDTA, 100 mM sucrose, and protease inhibitors) and transferred to Dounce homogenizer for 40-stroke homogenization. The samples were further homogenized by 10 passage of 25G needle, and the high efficiency of cell lysis were confirmed with 1:1 trypan blue staining under light microscope. The homogenate was layered onto a sucrose gradient solution comprised of 1.3 mL layers of the buffers (10 mM HEPES, pH 7.4, 1 mM EDTA) containing the following: 0.25, 0.5, 0.75, 1.0, 1.25, 1.5, 1.75, 2.0 M sucrose. The gradient samples were subjected to 200,000 xg for 18 h at 4°C. 0.65 mL of each fraction were collected from the top for subsequent immunoblotting and lipidomics analyses.

Isolation of SH-SY5Y cell membrane rafts

The isolation of membrane rafts was modified from published protocol (Boesze-Battaglia, 2006). In brief, ten 100 mm-plates of SH-SY5Y cells were harvested at 80% confluency. After washed twice with PBS, SH-SY5Y cells were scrapped and suspended in 1.1 mL MOPS buffer. 1 mL of cells were transferred to glass homogenizer on ice, and ice-cold 2% (v/v) Triton X-100 in MOPS buffer were added to the cell suspension. After homogenized with 15 strokes on ice, the homogenates were incubated on ice for 15 min. 1.24 mL of 2.4M sucrose in MOPS buffer were added to the homogenates and vortexed immediately. The samples were transferred to clear SW-41 centrifuge tubes on ice, and 1 mL of each of the following: 0.8, 0.7, 0.65, 0.6, and 0.5 M sucrose solutions were layered onto the sample to create a sucrose step gradient. The sucrose gradient layers were topped by MOPS up til approx. 0.10 cm from the top of the centrifuge tube and subjected to 200,000 xg centrifugation for 20 h at 4°C. The resultant samples were collected sequentially as 1 mL fractions from the top and subjected to immunoblotting analysis. The fractions containing isolated membrane rafts were concentrated at least 10x by centrifugal filter tube (Vivaspin® Turbo 4 Ultrafiltration. Sartorius), and subjected to immunoblotting.

Amplex Red-HRP assay

The Amplex Red fluorescent probe activated by horseradish peroxidase (HRP) was used for H_2O_2 detection. The experiment was performed according to the manufacturer's instructions (A22188, Invitrogen). In short, the reaction mixture containing 50 μM Amplex Red and 0.1 U/ml HRP was prepared in HBSS buffer. 100 μL/well of the reaction mixture were pipetted into 96-well plate and warmed at 37°C for 10 min. 20 μL of $2*10^4$ cells in HBSS buffer were added to the well, and the fluorescence (excitation: 545 nm; emission 590 nm) were recorded by Spectra Max i3x plate reader (Molecular Devices).

Rac1-liposome binding assay

For liposome preparations, lipid mixtures were dried and rehydrated in Buffer 1 [10 mM HEPES (pH 7.5), 140 mM NaCl, and 1.5 mM $MgCl_2$]. The lipid compositions for liposomes mimicking membrane-raft and autophagosome are listed below in percentage, and the total concentration of lipid mixture was 1 mM.

Membrane raft-like liposomes (del Pozo et al., 2004)					**Autophagosome-like liposomes** (Rao et al., 2016)						
PC	SM	Cho	Cer	DhCer	PC	PS	Cho	PE	PI3P	Cer	DhCer
33	33	33	0	0	57.5	10	20	10	2.5	0	0
30	30	30	10	0	47.5	10	20	10	2.5	10	0
30	30	30	0	10	47.5	10	20	10	2.5	0	10

Next, the liposome mixtures were subjected to a series of freeze-thaw cycles before being extruded through 0.1 μm pore size polycarbonate membranes (Whatman, Cat. 800309) using Avanti Mini-Extruder. C18 ceramide and dihydroceramide were used since C18 ceramides are the predominant species in the neuronal context (Laviad et al., 2008).

Recombinant Rac1 (Abcam, ab51014) was incubated with 1x GTPγS (Sigma, 20-176) or GDP (Sigma, 20177) in Buffer 2 [40 mM HEPES (pH7.5), 4 mM EDTA, 2 mM DTT] for 10 minutes at 30°C. The resultant protein mixtures were prenylated by rabbit reticulocyte lysate (Promega, L415A) and 2 μM farnesyl pyrophosphate (Sigma, F6892) in Buffer 3 (50 mM Tris, pH 7.5, 5 mM $MgCl_2$, 50 μM $ZnCl_2$ 2 mM DTT) for 30 min at 37°C. To determine membrane binding, prenylated Rac1 (1 μg) was added to 100 μL of 1 mM liposomes and incubated for 30 minutes at 37°C. Prenylated Rac1 protein was separated into soluble and membrane-bound fractions by 40,000 x g, 15-minute centrifugation at 4°C. Liposome pellets were washed 3 times with Buffer 1 before heating at 95°C for 10 min with 50 μL of 1x Laemmli Sample Buffer for western blotting.

QUANTIFICATION AND STATISTICAL ANALYSIS

Quantitative data were analyzed using two-tailed unpaired Student's t test, one-way ANOVA with Tukey's multiple comparison test, or two-way ANOVA with Šídák multiple comparison test and graphs were generated using GraphPad Prism 9.0.0. All data in bar graphs were expressed as mean ± SEM. P values of less than 0.05 were considered statistically significant.